Theory and Applications of Thermoplasmonics

John Miller

University of Arizona- Wyant College of Optical Sciences

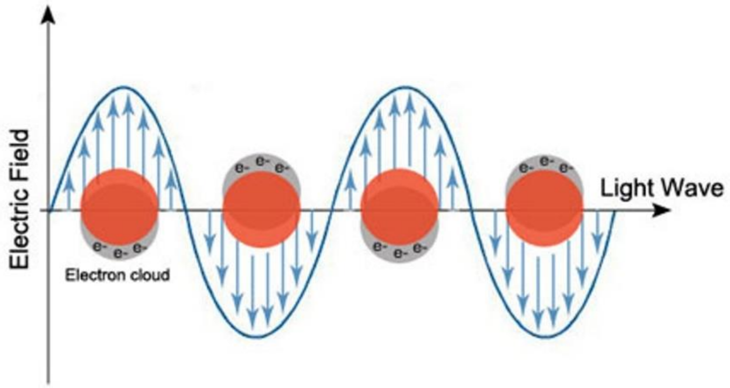

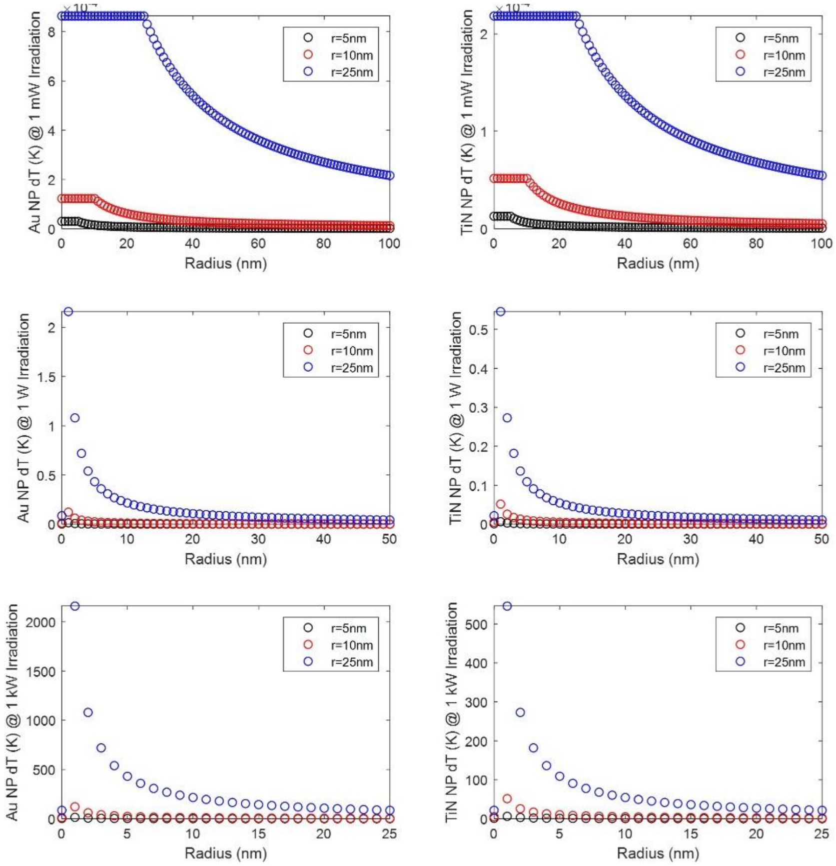

Table of Contents 2

Abstract 3

1. Plasmons, Surface Plasmon Polaritons, and Localized Surface Plasmons 4
    1.1 Plasmons 4
    1.2 Surface Plasmon Polaritons 5
    1.3 Localized Surface Plasmon Polaritons 13
2. Synthesis, Fabrication, and Materials for Plasmonic Nanostructures 23
    2.1 Synthesis and Fabrication of Plasmonic Nanostructures 23
    2.2 Materials for Plasmonic Applications 24
3. Theory of Thermoplasmonics 26
    3.1 Thermodynamic and Heat Transfer Models 26
    3.2 Measuring Temperature with Plasmonic Nanostructures 33
4. Applications of Thermoplasmonics 41
    4.1 Biomedical Applications 41
    4.2 Chemical Applications 42
    4.3 Solar Desalination Applications 46
    4.4 Thermophotovoltaic Applications 49
    4.5 Photoacoustic Imaging Applications 51
    4.6 Defense Applications 52
5. Conclusion 56
6. Appendix 57

Abstract

Plasmons are quanta of plasma oscillations arising from the charge density within a metal or other conducting material. Surface plasmons are plasma oscillations generated between metallic structures on the surface of a dielectric material. Examples include surface plasmon polaritons, where surface plasma waves propagate along a continuous metal/dielectric interface, and localized surface plasmons which are isolated arrays of metallic nanostructures where the metallic nanostructures oscillate in place and are not free to propagate. Traditionally, plasmonic structures have been investigated for their ability to confine light to dimensions smaller than the diffraction limit of light. These metallic nanostructures also can generate nanoscale quantities of heat upon optical initiation, particularly at their resonant optical frequency. Thermoplasmonics is the study of how plasmonic nanostructures can be utilized to generate heat for various applications to boost heat generation. The purpose of this report is to discuss the theory of plasmonics and its relationship to thermoplasmonics. Basics of plasmons, surface plasmon polaritons, and localized surface plasmons are discussed in detail and derivations of key equations are summarized. Then properties of key plasmonic materials and methods of synthesizing or fabricating plasmonic structures are discussed. After the fundamentals are established, mechanisms of heat transfer in thermoplasmonics are discussed and key equations describing heat transfer in thermoplasmonic structures are described as well as imaging techniques for measuring heating due to plasmonic structures. Finally, various applications and benefits of plasmonic nanostructures are discussed for various fields, including the biomedical, chemical, energy, and defense industries. Throughout the paper the plasmonic properties of several key metallic thin films, including gold, silver, and titanium nitride, are evaluated from published refractive index data for enhancing understanding of material plasmonic properties and how their shape and structure affect their material optical properties.

1. Plasmons, Surface Plasmons Polaritons, and Localized Surface Plasmons

1.1 Plasmons

Plasmonic nanostructures are incredibly interesting materials to researchers due to their ability to confine light below the diffraction limit and have various applications in biotechnology, imaging, spectroscopy, and photovoltaics just to highlight a few. Plasmons are discrete quanta of a plasma oscillation like photons are quanta of electromagnetic wave oscillations and phonons are quanta of mechanical vibrations in solids. A plasma oscillation is an oscillation of charge density in a material (most of the time a metal or heavily doped semiconductor) where the electron cloud in a material (atom, thin film, cluster, etc.) segregates to one side of the atom creating a charged dipole between the electron cloud and the positively charged nuclei of the material/material cluster. This field moves back and forth creating the dipole oscillation known as the plasma oscillation, until the energy supplied is dampened, at a plasma frequency specific to the material,

$$\omega_p = \sqrt{\frac{Ne^2}{\epsilon_o m^*}} \tag{1}$$

where N is the carrier concentration (the carriers are electrons in the case of plasmonic materials), e is the elementary charge, ϵ_o is the permittivity of free space, and m^* is the effective mass of the free carrier. This frequency is critical for understanding the optical properties of metals, as frequencies of light incident above the plasma frequency are typically transmitted into a material and frequencies below the plasma frequency are typically reflected, because the material acts like a perfected electrical conductor (PEC). The plasmon energy is related to the plasma energy through planks constant and can be estimated as,

$$E_p = \hbar\omega_p \tag{2}$$

which is derived from the free electron model [1-3].

1.2 Surface Plasmon Polaritons

Plasmons can be localized to a thin region of a material creating a surface plasmon. Typically, surface plasmons represent a plasma oscillation in a metal along a metal/dielectric interface, where the real part of the dielectric function changes from positive to negative when coupled to an incident optical source. There are two types of surface plasmons: surface plasmon polaritons (SPP's) and localized surface plasmons (LSP's). In a surface plasmon polariton, an optical beam is incident on a thin metallic film deposited through a dielectric interface, forming a plasmonic surface wave that propagates along the metallic/dielectric interface [1-3]. Figure 1 demonstrates how a surface plasmon polariton forms along the metal/dielectric interfaces behaves upon optical irradiation [4]. The benefit of this technique is that the light can be confined to dimensions smaller than the diffraction limit of light.

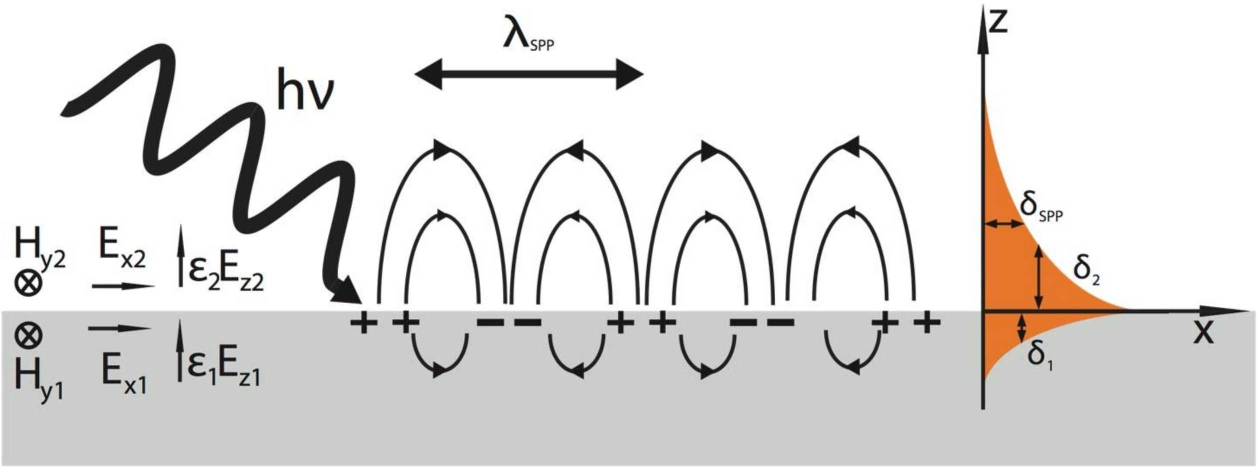

Figure 1. Surface plasmon wave formed between a metal/dielectric interface when coupled with an optical source, forming a surface plasmon polariton [4].

The plasmonic properties of metallic materials are determined by their dielectric functions or optical dispersions. The complex dielectric functions, and therefore the optical dispersions, of metallic materials are described by the Lorentz-Drude Model,

$$\epsilon(\omega) = 1 - \frac{{\omega_p}^2}{\omega^2 + i\omega\gamma} \tag{3}$$

where γ is the damping or relaxation coefficient. The Lorentz-Drude model is a simplification of the classical Lorentz-Oscillator model,

$$\epsilon(\omega) = 1 + \frac{{\omega_p}^2}{{\omega_o}^2 - \omega^2 - i\omega\gamma} \tag{4}$$

where ω_o is the resonant frequency. The Lorentz Oscillator model describes the interaction of atoms under an electric field, in this case an optical electromagnetic wave, as electrons bound to atoms with springs. Atoms are polarized due to optical irradiation and the displacement is restored due to a spring force between the positively charged nucleus and the electrons. In a metal the conduction electrons that are free to flow through the "sea of electrons" described by metallic bonding, are not bound to the positively charged nucleus, and therefore the resonant frequency is not included [2,3,5]. The complex dielectric constant is related to the complex refractive index or optical dispersion by the following relation,

$$n = \sqrt{\varepsilon} \tag{5}$$

where n and ε have both real (n_r and ε') and imaginary components (k_i and ε"). Figures 2 and 3 show the real and imaginary components of the dielectric constant and refractive indices of titanium nitride (TiN), silver (Ag), and gold (Au), a few metallic materials with plasmonic properties, as both a function of the incident free space wavelength and photon energy, acquired through external references [6-8]. In this report, plasmonic properties of materials are mostly described as a function of the incident photon energy. Table 1 shows some useful relationships between the free space wavelength, free space wavevector, free space angular frequency, and photon energy for a few fundamental wavelengths/frequencies in optical science to serve as reference. Dielectric media can also have their optical dispersion modeled as a Lorentz oscillator, but simpler empirical models for the refractive index are typically employed, such as the Cauchy model in the visible region of the optical spectrum or the Sellmeier model for extending the region to the near infrared region and for anomalous dispersions [9].

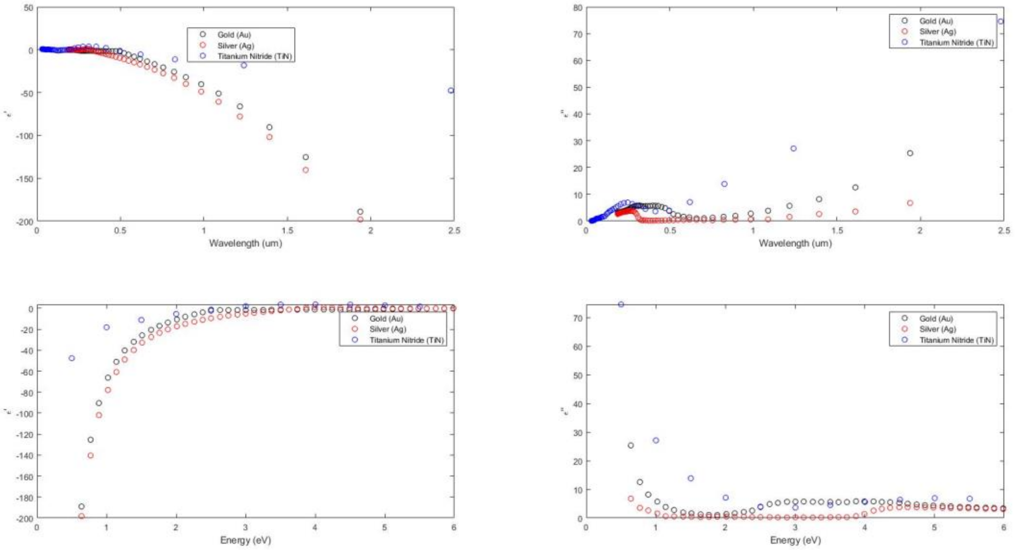

Figure 2. Real and imaginary components of the dielectric constants of gold, silver, and titanium nitride as a function of both the free space wavelength and the incident photon energy [6-8]

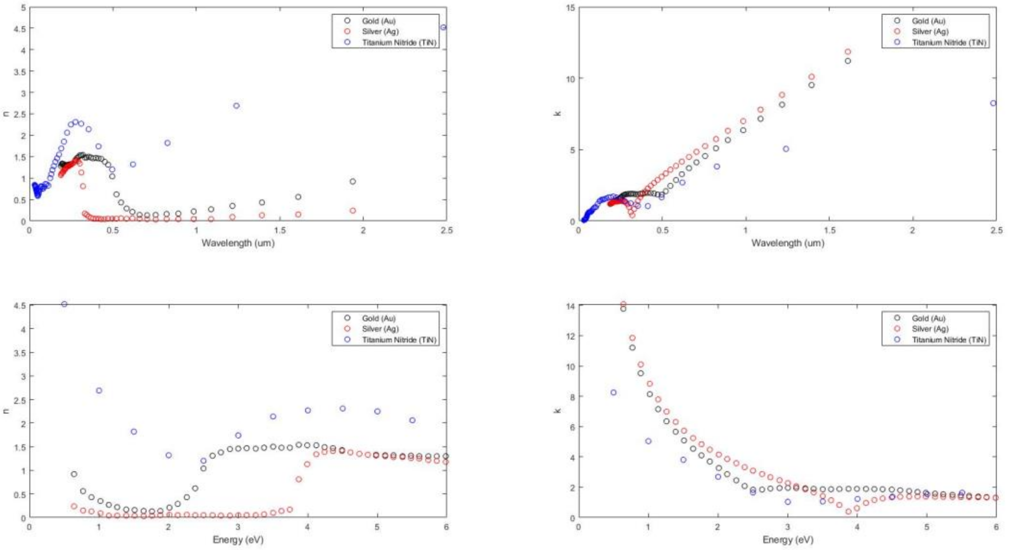

Figure 3. Real and imaginary components of the dielectric constants of gold, silver, and titanium nitride as a function of both the free space wavelength and the incident photon energy [6-8]

Table 1 Comparison of the free Space wavelengths, wavevector magnitude, angular frequency, and photon energy of a few characteristic frequencies in optical science.

Wavelength (nm)	Wavevector (cm^{-1})	Angular Frequency (Hz)	Photon Energy (eV)	Characteristic
380	165347	4.96E15	3.26	Lower Bound of Visible Light Range
532	118105	3.54E15	2.33	Fundamental Wavelength of Frequency Doubled YAG, Common Laser Diode Wavelength
632.8	99292	2.98E15	1.96	Fundamental Wavelength of HeNe Laser
750	83776	2.51E15	1.65	Upper Bound of Visible Light Range
808	77762	2.33E15	1.54	Resonant Absorption Wavelength for Nd:YAG, Common Laser Diode Configuration
1064	59053	1.77E15	1.17	Fundamental Emission Wavelength of Nd:YAG
1550	40537	1.23E15	0.80	Telecom Operation Wavelength

Typically, a material's plasmonic properties can be evaluated by a quality factor which balances the plasmonic performance of the material (negative real part of the dielectric function) with its optical losses through absorption (imaginary portion of the dielectric function) [10]

$$Q_{SPP} = \frac{\epsilon'^2}{\epsilon"} \qquad (6)$$

Figure 4 summarizes the quality factors for gold, silver, and titanium nitride metallic films as a function of wavelength and photon energy. Quality factors and other plasmonic properties discussed in this work are calculated from the refractive index and dielectric functions discussed above. [6-8] From the figure we can see that silver has the highest quality factor followed by gold, and then titanium nitride, which is a very poor plasmonic material. This is driven by the ratio of the high dielectric response from the real part of the dielectric function compared to the optical losses driven by the imaginary part of the dielectric function. The quality factor also goes up as a function of increasing free space wavelength in all cases (decreasing photon energy) due to the increasing rate of change of the negative real part of the dielectric function relative to the imaginary portion.

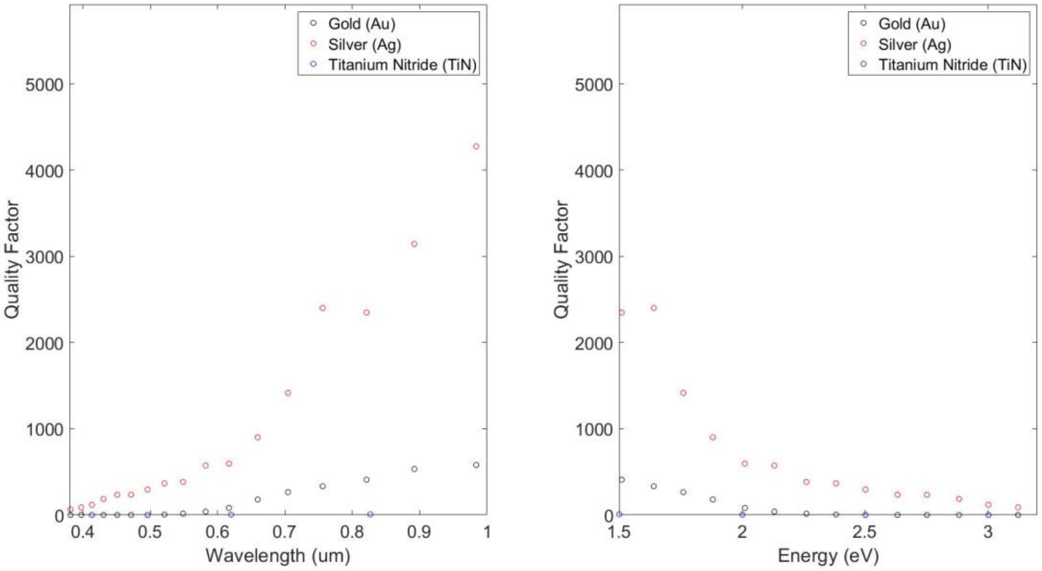

Figure 4. Quality factors of gold, silver, and titanium nitride plasmonic metals as a function of both the free space wavelength and photon energy

Surface plasmon polaritons are surface plasma waves propagating along the metallic/dielectric interface generated from an external electric field, such as optical irradiation. The surface plasmon polariton dispersion relation is derived from Maxwell's Equations (specifically Ampere's Equation) assuming the normal components of the displacement (D) and magnetic flux density (B) and the tangential components of the electric (E) and magnetic field strength (H) are continuous at the dielectric/metal interface,

$$k_x^2 = \left(\frac{\omega}{c}\right)^2 \left(\frac{\varepsilon_1 \varepsilon_2}{\varepsilon_1 + \varepsilon_2}\right) \tag{6}$$

Or

$$k_x' + k_x'' i = \left[\frac{\omega}{c}\left(\frac{\varepsilon_1' \varepsilon_2}{\varepsilon_1' + \varepsilon_2}\right)^{\frac{1}{2}}\right] + i\left[\frac{\omega}{c}\left(\frac{\varepsilon_1' \varepsilon_2}{\varepsilon_1' + \varepsilon_2}\right)^{\frac{3}{2}} \frac{\varepsilon_1''}{2\left(\varepsilon_1'\right)^2}\right] \tag{7}$$

If broken up into real and imaginary components where the surface plasmon propagation is along the x-direction, ε_1 is the dielectric function of the metal, and ε_2 is the dielectric constant of the dielectric material [1-3]. Typically, the dielectric media is considered to be loss-less so the imaginary component of the dielectric constant is often neglected. Figure 5 shows the real and imaginary part (both the wavevector and inverse wavevector) of the polariton dispersion as a function of incident energy for gold, silver, and titanium nitride utilizing the dielectric function data above and assuming the dielectric material is glass (n_2=1.5 and ε_2=2.25). [6-8] The real part of the polariton dispersion describes the maximum spatial frequency of oscillation achievable (or minimum length of plasma oscillation) and the imaginary part describes the decay of the surface plasmon through attenuation, typically by the metal. As shown in Figure 5, the size of the polariton decreases with increasing photon energy (shorter wavelengths), but so does the attenuation for each material system. Figure 5c. overlays the corresponding free space wavelength which shows the polaritons can be generated smaller than the free space wavelength. It is important to note that in order to couple the incident wavelength dispersion to the polariton dispersion, the light must be coupled through the dielectric media, and not the air side, so that the dispersion of optical radiation can overlap with the surface plasmon dispersion relation. In all cases the polariton size decreases with increasing energy, though silver can achieve the smallest SPP lengths. For the silver SPP the minimum polariton size is reached when the plasmon energy is 3.37 eV (corresponding to a vacuum wavelength of 368 nm) of 110.6 nm.

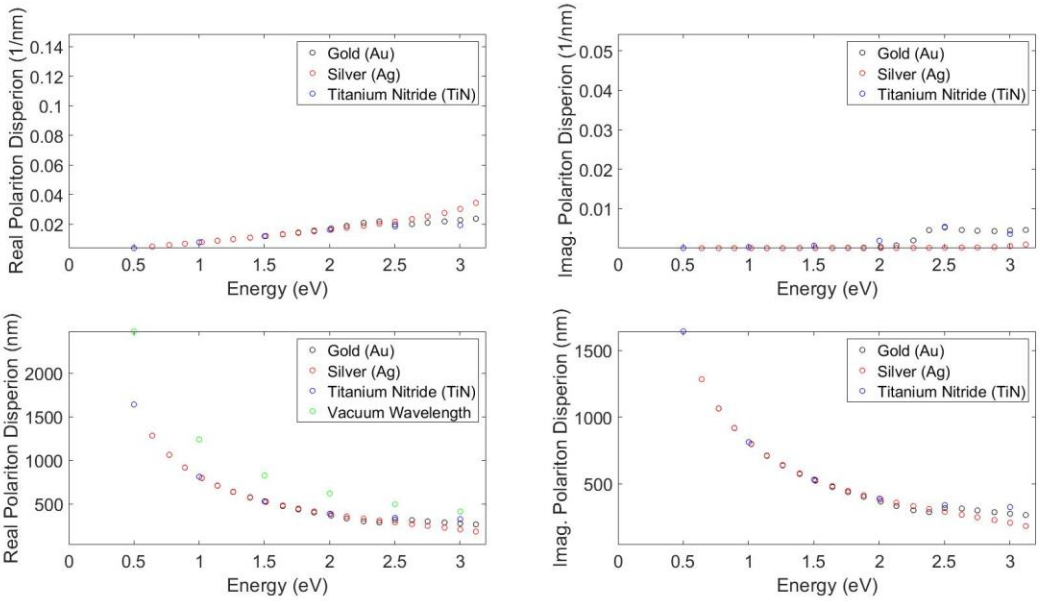

Figure 5. Real and imaginary components of both the polariton wavevector and wavelength for gold, silver, and titanium nitride

Other key metrics of the surface plasmon polariton are the decay length and penetration length in each media (skin depth),

$$\delta_{SPP} = \frac{1}{2k_x''} \qquad (8)$$

$$\delta_d = \frac{1}{k_o} \left| \frac{\varepsilon_1' + \varepsilon_2}{\varepsilon_2^2} \right|^{1/2} \qquad (9)$$

$$\delta_m = \frac{1}{k_o} \left| \frac{\varepsilon_1' + \varepsilon_2}{(\varepsilon_1')^2} \right|^{1/2} \tag{10}$$

where the decay length describes the distance the surface plasmon wave travels along the interface before the amplitude decays by 1/e and the penetration length describes the penetration in the z-direction into the metallic and dielectric media (normal to the metallic coating interface) [1]. Figure 6 shows the surface plasmon decay length for each metal of interest. Silver has the highest decay length, attributed to low losses, followed by gold, and then titanium nitride, whose plasmon decay length is small, even with lower incident optical beam coupling. For all material cases, the decay length shortens with increasing optical photon energy. In terms of device design, this provides an optimization challenge that can vary based on the application of the device, where shorter polaritons decay over shorter lengths, shrinking devices. This could lead to limitations in device design due to capabilities of modern manufacturing techniques for developing plasmonic devices. Figure 7 shows the penetration depths of the surface plasmon in both the metallic and dielectric media, as well as the relative ratio of plasmon penetration depths in the dielectric vs. metal. As demonstrated by the figure, decay in the dielectric media is much lower than in the metal due to low attenuation. Table 3 in the appendix summarizes surface plasmon polariton performance at several incident photon energies in the visible and near infrared region of the optical spectrum for gold, silver and titanium nitride.

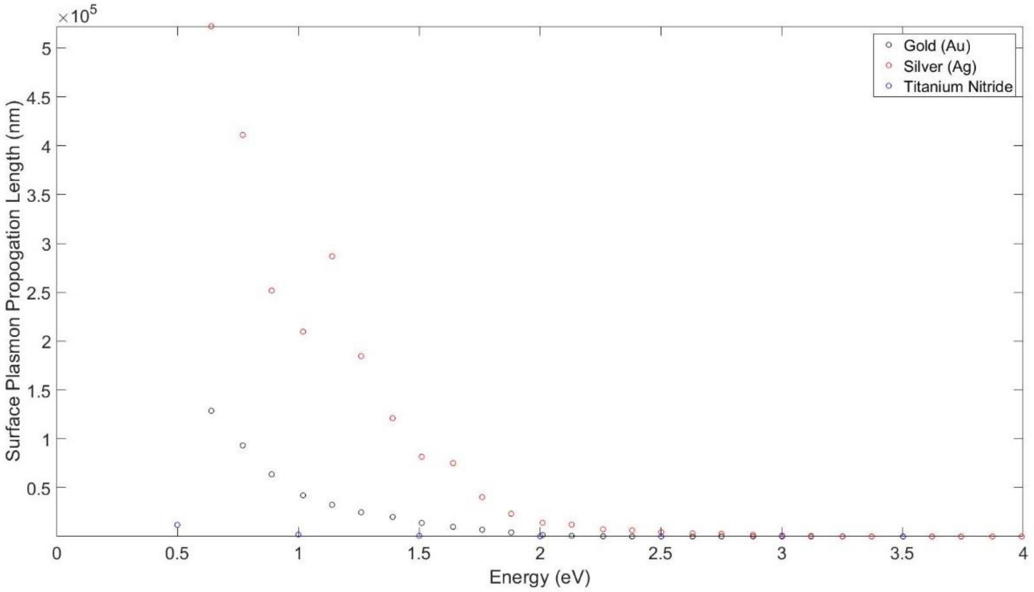

Figure 6. Surface plasmon propagation length in terms of the incident photon energy for gold, silver, and titanium nitride

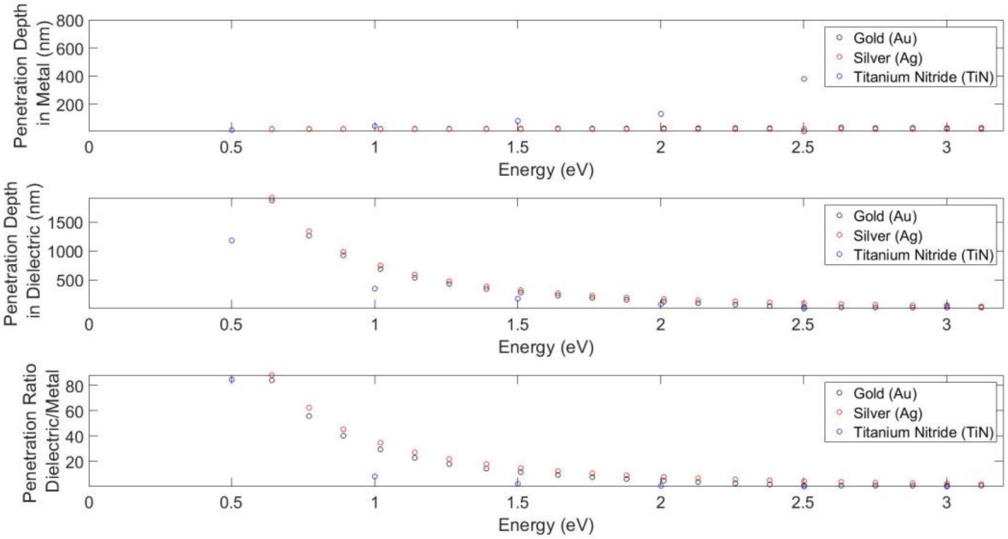

Figure 7. Skin depths of surface plasmon waves in metal (top), dielectric (middle), and the ratio of penetration between dielectric and metal (bottom) for gold, silver, and titanium nitride

1.3 Localized Surface Plasmons

Localized surface plasmons are arrays of metallic nanostructures deposited onto or embedded into a dielectric matrix. They differ from surface plasmon polaritons in the fact that the plasmon waves cannot propagate along the metal/dielectric interface, and so the plasmonic nanostructures oscillate in place. These localized surface plasmons can be utilized for enhancing optical absorption and scattering [1-3]. A diagram of localized surface plasmons in metallic nanoparticles under optical irradiation can be seen in Figure 8, where the electron cloud oscillates back and forth around the positively charged nucleus [11].

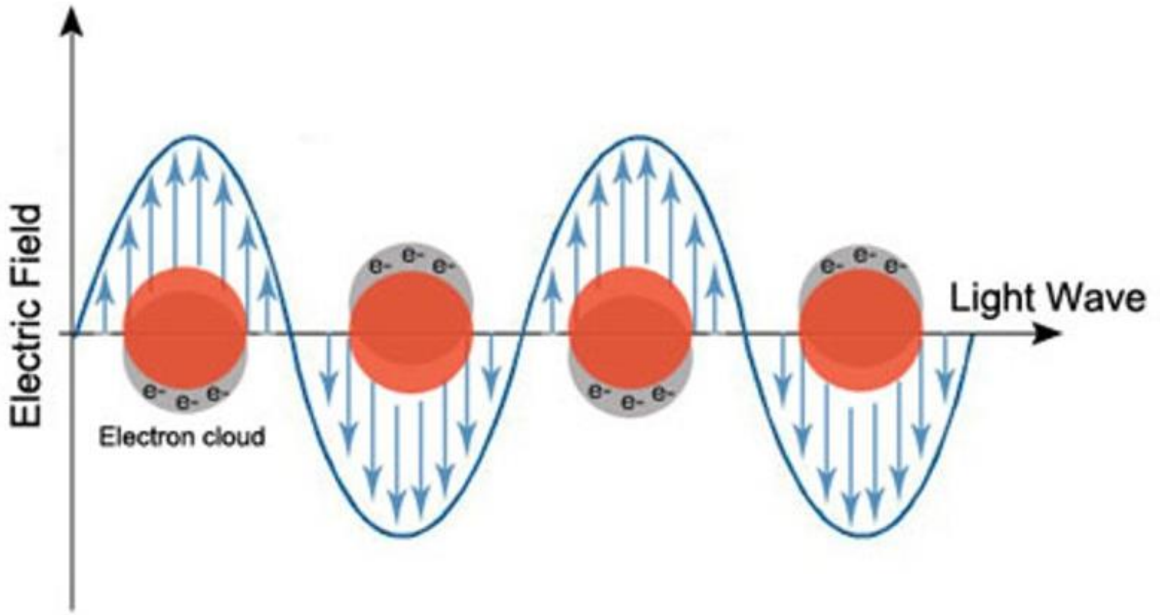

Figure 8. Localized surface plasmon of metallic nanoparticles formed under an electric field during optical irradiation [11]

Similar to the surface plasmon polariton modes, materials used for localized surface plasmons are described by a slightly modified quality factor in terms of the real and imaginary components of their dielectric function [10]

$$Q = \frac{-\varepsilon'}{\varepsilon''} \tag{11}$$

Figure 9 shows the LSPR quality factor for silver, gold, and titanium nitride as a function of both incident wavelength and photon energy. Like the quality factors measured for the surface plasmon polaritons, silver demonstrates the highest quality factor, followed by gold and then titanium nitride. Peak quality factors for each material are demonstrated in the near infrared region of the optical spectrum.

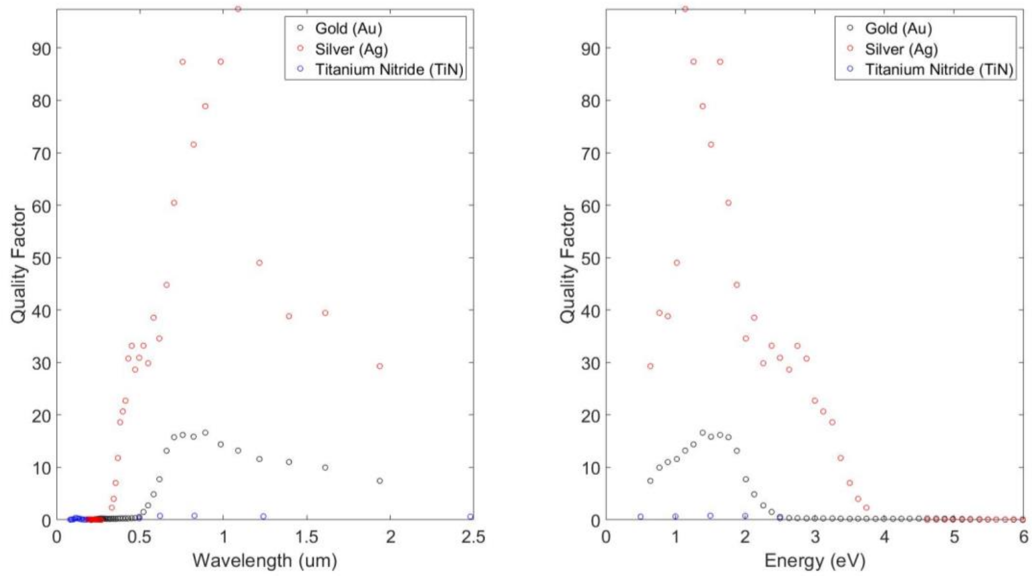

Figure 9. Quality factors for the localized surface Plasmons for gold, silver, and titanium nitride as a function of incident wavelength and photon energy

For spherical nanoparticles, whose dimensions are of a size on the order of the incident optical wavelength, the scattering, absorption and extinction cross sections are given by Mie Theory, a theory based on a solution to Maxwell's equations that typically is used to describe scattering of light in the atmosphere. Mie theory assumes uniformly distributed particles in isotropic media and differs from Rayleigh scattering based on the size of the particles, where Rayleigh scattering describes scattering when particles are much smaller than the incident wavelength of light [1]. Plasmonic nanostructures can consist of structures other than spheres (cubes, pyramids, nano-antennas, nano-wires, etc) and other more complicated models have been developed and simulated to describe absorption and scattering cross sections [1,12]. Figure 10 shows the extinction, absorption, and scattering cross sections of different metallic nanostructure shapes as a function of wavelength. As shown in the figure, by tuning the nanostructure shape, the position of the resonance peak, the number of resonances, and the broadening of the resonance peak can be adjusted. For example, by controlling the number of faces on the object the number of resonances increases because the number of ways the structures are polarizable increases [1,15].

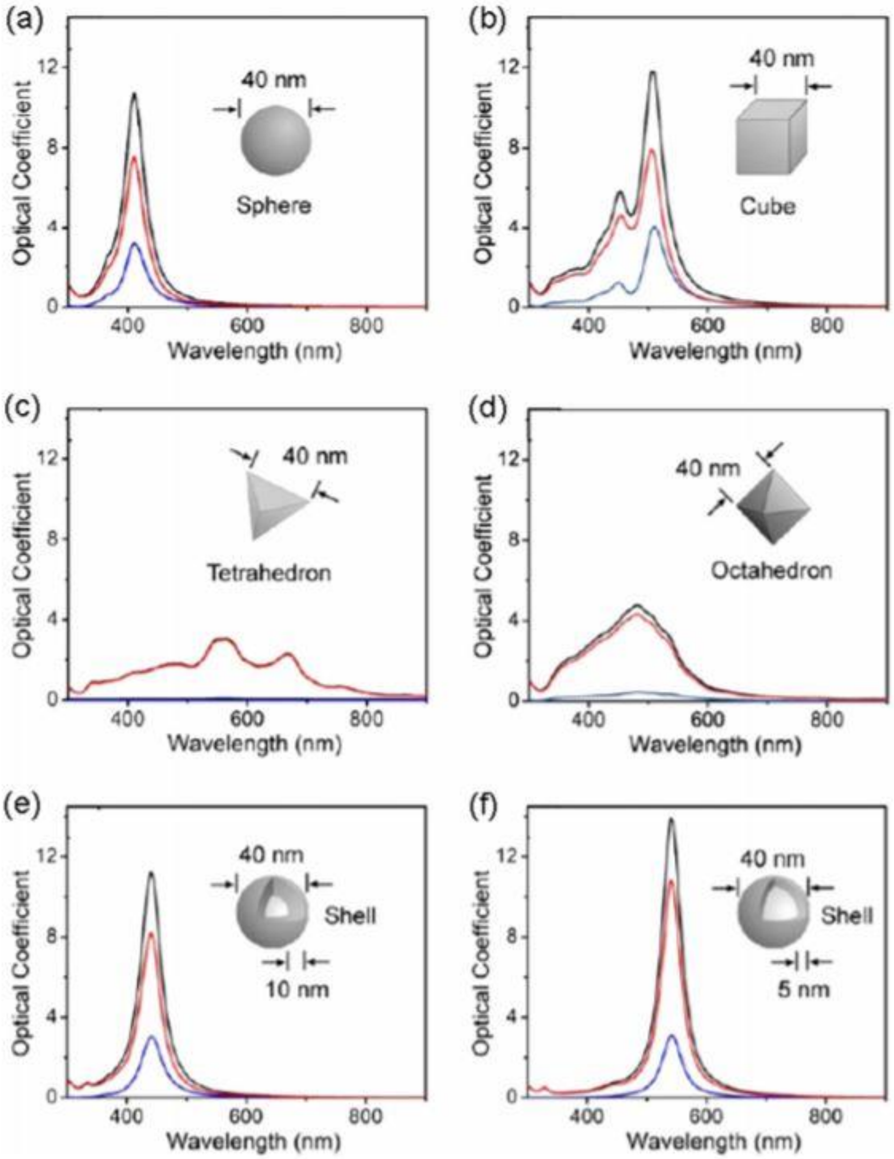

Figure 10. Extinction (black), absorption (red), and scattering (blue) cross sections of different nanoparticle shapes [1]

From Mie theory, the cross sections derive from the polarization of the metallic nanospheres under an incident electric field (laser beam),

$$P = \alpha E_{inc} \tag{12}$$

where P is the polarization, α describes the electronic polarizability, and E_{inc} is the electric field applied from the incident optical source [13]. The Clausius-Mossotti electronic polarizability for metal nanoparticles is described by the dipolar approximation,

$$\alpha = 4\pi r^3 [\frac{\varepsilon_1(\omega)-\varepsilon_2}{\varepsilon_1(\omega)+2\varepsilon_2}] \tag{13}$$

for a sphere where r is the radius of the nanostructure. For larger particles a correction factor is typically included where the polarizability reads

$$\alpha = \left[\frac{\alpha_o}{1-\left(\frac{2}{3}\right)ik^3\alpha_o}\right] \tag{14}$$

where α_o is the original Clausius-Mossotti electronic polarizability [13, 14]. Different shapes have different functions that describe the polarizability of the metallic nanostructures. Figure 10 shows the real and imaginary components of the electronic polarizability of both gold and titanium nitride, assuming spherical geometries. As seen from the figure gold has a much higher degree of polarizability than titanium nitride, owing to its better performance as a plasmonic material. The polarizability is most intense between 1.5 and 2.5 eV for gold and between 0 and 6 eV for titanium nitride, a much broader band absorber.

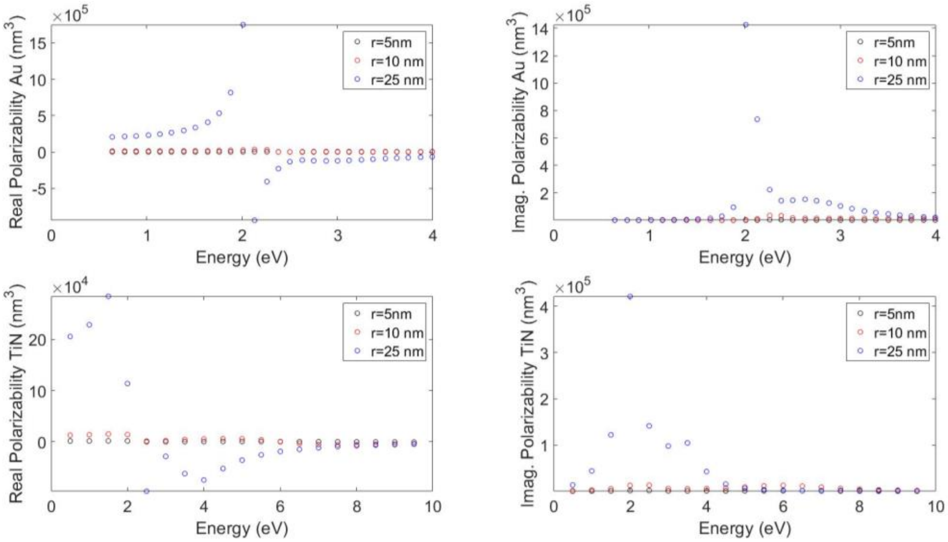

Figure 11. Real and imaginary components of the electronic polarizability of gold and titanium nitride

The cross sections for scattering, extinction, and absorption as described by Mie Theory for single spheres are then given by

$$C_{ext} = \frac{4\pi k_o}{|E_{inc}|^2} Im(E_{inc}^{*}.P) = k_o Im(\alpha) \tag{15}$$

$$C_{sca} = \frac{8\pi k_o^4}{3|E_{inc}|^2} |P|^2 = \frac{k_o^4}{6\pi} |\alpha|^2 \tag{16}$$

$$C_{abs} = C_{ext} - C_{sca} \tag{17}$$

for singular particles where k_o describes the incident wavevector ($\lambda_o=2\pi n_o/k_o$) [1,13,14]. Typically to enhance absorption and scattering resonances, arrays of nanoparticles experiencing a collective dipole moment are utilized, with more complicated cross section equations for the collective resonance,

$$C_{ext} = \frac{4\pi k_o}{|E_{inc}|^2} \sum_{j=1}^{N} Im(E_{inc}^{*}.P) \tag{18}$$

$$C_{sca} = \frac{k_o^4}{|E_{inc}|^2} \int d\Omega \, | \sum_{j=1}^{N} |[P_j - \hat{n}(\hat{n} \cdot P_j)] \exp\left(-ik_o \hat{n} \cdot r_j\right) |^2 \tag{19}$$

$$C_{abs} = \frac{4\pi k_o}{|E_{inc}|^2}\sum_{j=1}^{N}\{Im(P_j \cdot \left(\alpha_j^{-1}\right)^{*} P_j^{*} - \frac{2}{3}k_o^3 P_j \cdot P_j^{*}\} \tag{20}$$

More complicated absorption and scattering cross sections can be simulated using computational techniques like the discrete dipole approach, finite, difference time-domain methods, and finite element methods. These methods were not explored in detail in this report [1]. Figures 11, 12, and 13 show the total and normalized extinction, scattering, and absorption cross sections for gold and titanium nitride nanoparticles at several different particle sizes (10nm, 20 nm and 50 nm diameter or 5 nm, 10 nm, or 25 nm radius) on a glass substrate (n=1.5). Extinction is defined as the total optical loss either due to scattering or absorption of the incident photon energy/wavelength. As seen in Figure 11, the total optical extinction cross section significantly increases with particle size, along with red-shifting the extinction resonance peak (shifting of resonance to lower photon energies or longer wavelengths). The extinction cross section of gold is also nearly three times greater than that of titanium nitride owing to its enhanced dielectric properties from a higher magnitude dielectric function.

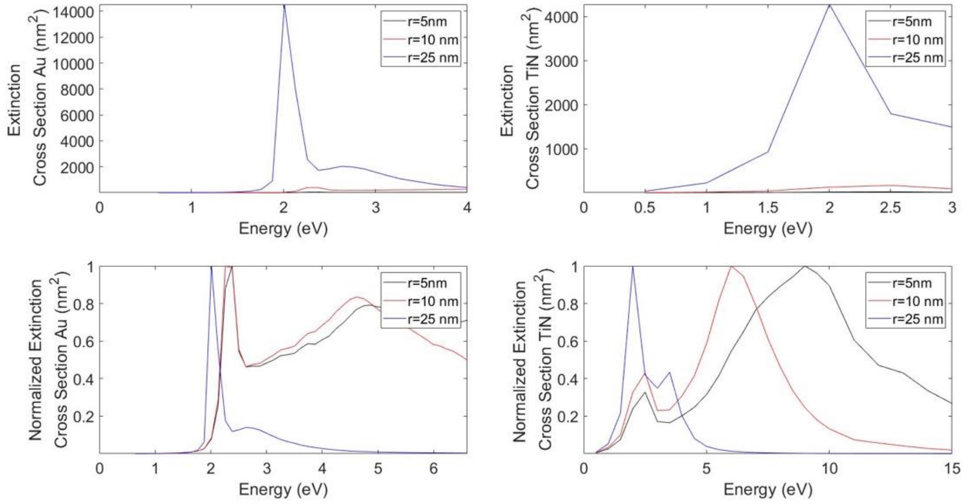

Figure 12. Total and normalized extinction cross section of gold and titanium nitride

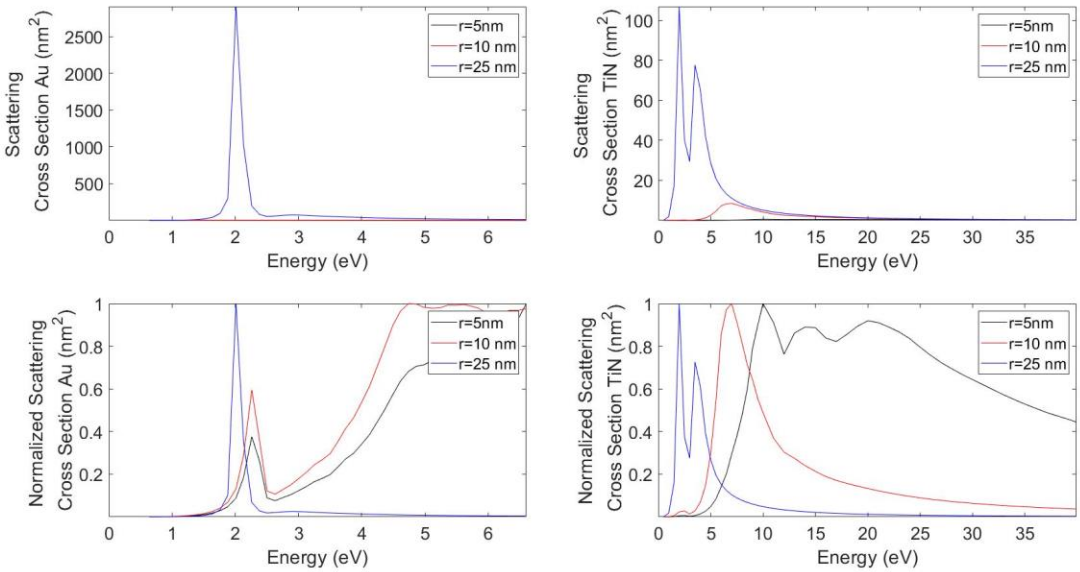

Figure 13. Total and normalized scattering sections of gold and titanium nitride

Figure 12 shows the total and normalized scattering cross sections for both gold and titanium nitride nanoparticles as a function of incident photon energy at several different particle sizes. Cross sections show that scattering is nearly insignificant in small particles, only becoming significant as the particle sizes approach 50 nm diameters in the visible region of light. Scattering is much more significant for smaller particles in the high energy photon regime (4-6 eV for gold and 5-40 eV for titanium nitride), corresponding to the ultraviolet regime of the frequency spectrum. These resonances red-shift towards the visible spectrum as the size of the particles increases for both the gold and titanium nitride particles.

Finally, Figure 13 shows the total and normalized absorption cross sections for both gold and titanium nitride particles as a function of incident photon energy at a few different particle sizes. Total extinction for both gold and titanium nitride are both dominated by absorption., which is significantly higher than scattering. The absorption red -shifts to lower photon energies (longer wavelengths) with increasing particle size. Resonance peaks also shift to narrower absorption bands as the metallic particle sizes increase. Table 4 in the appendix evaluates the absorption/scattering properties at their relative plasmonic resonant frequencies for gold and titanium nitride at various particle sizes (10 nm, 20 nm, 50 nm).

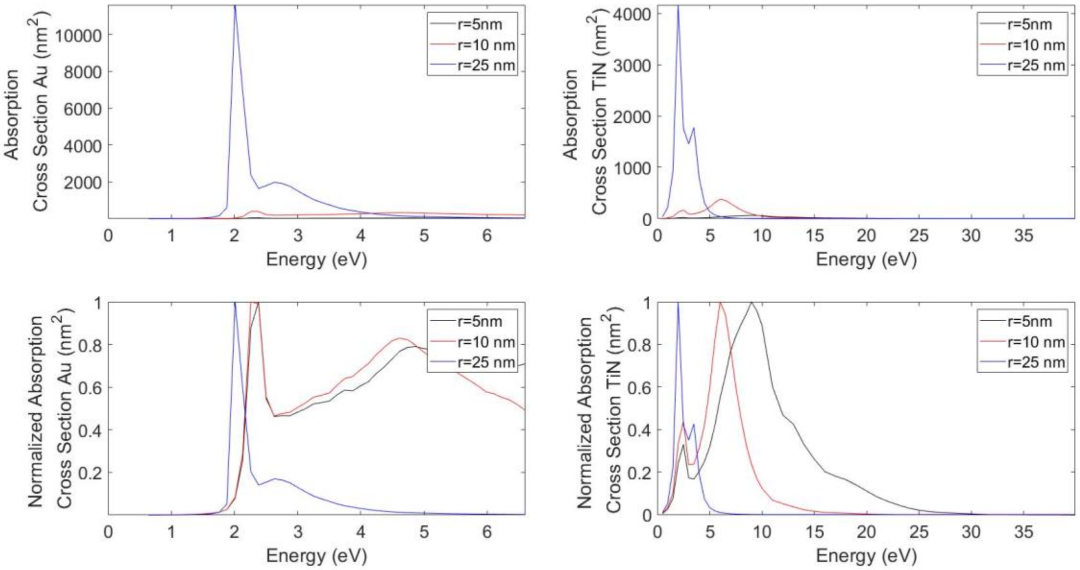

Figure 14. Total and normalized absorption cross section of gold and titanium nitride

For photothermal applications, plasmonic nanostructures can often be described by a photothermal efficiency, which compares the total absorption cross section of the nanostructure to the total extinction,

$$\mu_{ph} = \frac{C_{abs}}{C_{ext}} \tag{21}$$

where C_{abs} and C_{ext} represent the absorption and extinction cross sections, respectively. Figure 14 shows the photothermal efficiencies for both gold and titanium nitride. As seen in the figure, total photothermal efficiency decreases with increasing particle size due to increased contributions from scattering. Due to its intrinsic dielectric dispersion gold suffers a more significant decrease in photothermal efficiency, particularly along a resonance between 0.5 and 2.5 (NIR to Visible), compared to titanium nitride nanostructures, demonstrating titanium nitride's proficiency as a broad band absorber (though note that total absorption cross sections in gold are significantly higher).

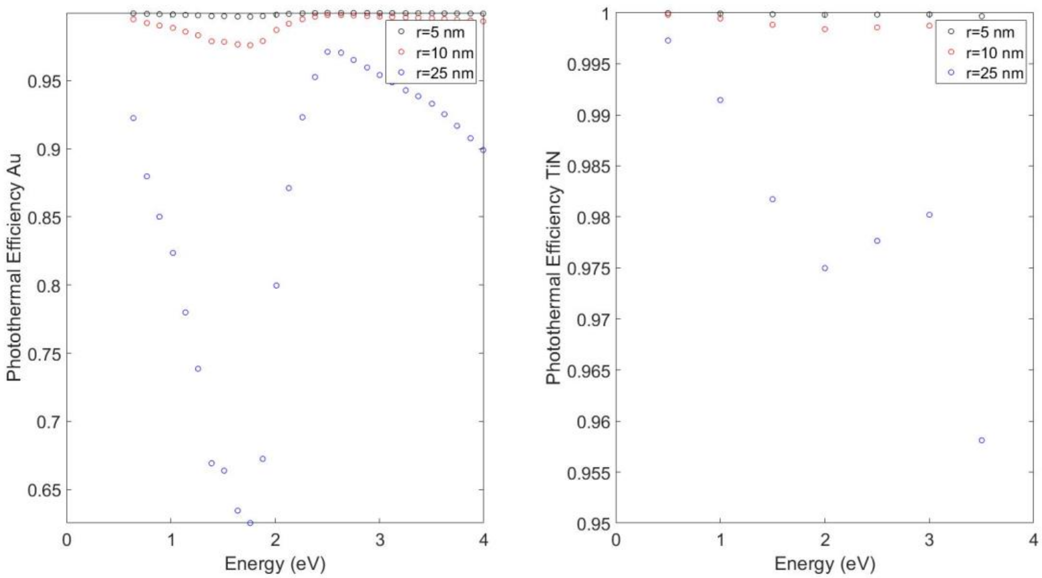

Figure 15. Photothermal efficiency of gold and titanium nitride

2. Synthesis, Fabrication, and Materials for Plasmonic Nanostructures

2.1 Synthesis and Fabrication of Plasmonic Nanostructures

Optimal properties of plasmonic materials are heavily dependent on their application. On top of the chemical and dielectric properties of the material, the properties of plasmonic nanostructures are also determined by their size, shape, and spatial distribution. Plasmonic structures for surface plasmon polaritons can be deposited onto dielectric media by common thin film metallization techniques such as magnetron sputtering, electron beam evaporation, and thermal evaporation. These techniques can be coupled to lithographic techniques to make unique structures for propagation on photonic devices. More complicated thin film structures based on alternating layers of metallic and dielectric layers have also been demonstrated [15]. Localized surface plasmons however are much more complicated and several advanced fabrication and development techniques have been employed, depending on whether the plasmonic nanostructures need to be deposited on the surface or embedded in the media of interest.

For deposition of materials directly on the surface of a dielectric media, the most facile way of generating localized plasmonic nanostructures is to simply apply, through a method like spin or dip coating, a metal nanoparticle solution on the surface of the dielectric material. The nanoparticle solution could either be commercially acquired or synthesized by reduction of a metallic salt (like silver chloride) into a metallic form [16]. Different wet chemical processes have been demonstrated for the synthesis of various nano-shapes including spheres, rods, triangles, and plates [16,17]. The wet chemical approach is also useful if it is necessary for the application to embed plasmonic materials into the component of interest, such as membranes for distillation. This way the metallic nanoparticle solution can be embedded directly during the synthesis/drying of the component of interest. While simple and low cost, this technique allows for minimal control over the nanostructure shape and array spacing. For better control of the shape, size, and array spacing more expensive lithography techniques, such as photolithography or e-beam lithography, are used for developing custom metallic structure dimensions on photoresist. [18] The limitation for these techniques, however, lies in the fact that nanostructures can only be deposited onto the surface of the material and cannot be embedded into the bulk, limiting their application space.

2.2 Materials for Plasmonic Applications

Since most conductive materials have a plasmonic response (depending on the size of their free carrier concentration), many material systems for plasmonic nanostructures are arising due to other chemical and structural properties. Gold and silver have long been considered the standard plasmonic materials due to their strong dielectric responses in the visible and near infrared range with low optical losses. Gold has the additional chemical benefit of being resistant to oxidation and biocompatible due to its inert nature, while silver has the benefit of relative abundance and therefore low cost. Materials like copper and aluminum also have strong plasmonic properties but suffer even worse than silver in terms of chemical degradation from oxidation. Due to the high energy density in aluminum nanotechnology, plasmonic aluminum structures have been investigated for defense applications in propellants and explosives [19]. Other noble materials like platinum and ruthenium are resistant to oxidation-based degradation and have strong catalytic properties like gold but have weak plasmonic properties attributed to a lower magnitude of the real part of their dielectric functions [1].

In addition to pure mono-atomic metal films, non-traditional plasmonic materials are being investigated for plasmonic applications. Transparent conducting oxides like indium doped tin oxide (ITO) and aluminum doped zinc oxide (AZO) are conductive materials that are transparent in the visible region of light, so they are being investigated for their plasmonic properties in the near infrared region of light. Another material system in the family of NIR plasmonics includes graphene, a two-dimensional, single layer of carbon arranged in a planar honeycomb structure. Graphene is interesting as a plasmonic material due to its low optical loss and the tunability of its plasmonic response by tuning its free carrier concentration through control of impurities and impurity levels [20-22]. A common application space for these materials is thermophotovoltaics as blackbody emitters, which will be discussed later. Refractory metal nitrides, such as zirconium nitride (ZrN) and titanium nitride (TiN), are also being investigated as broad band plasmonic absorbers due to their high thermomechanical strength. The interest lies in their ability to withstand high solar fluxes under concentrated solar illumination without damage whilst behaving like a broadband solar absorber. There is also interest in these materials for high laser fluence resistance in optoelectronic devices. [23-26] Finally, alloyed metallic materials (AgAu) are also an arising material system of interest for plasmonics work. By varying the composition, one can easily tune the plasmonic resonance frequency to a given value. [27]

3 Theory of Thermoplasmonics

3.1 Thermodynamic and Heat Transfer Models

Plasmonic materials are typically sought after because of their ability to confine light below the diffraction limit. Typical applications of plasmonic materials include bio-sensing, imaging, and lithography. In addition to their ability to confine light to smaller dimensions, plasmonic nanostructures can act as nano-sources of heat upon optical illumination. Thermoplasmonics is the study of how these plasmonic materials can generate and transfer heat upon illumination, with applications including photo-thermal cancer therapy, bio-sensing, catalysis, solar desalination, thermophotovoltaics, and optical initiation of insensitive high explosives. The primary mechanism of heating in plasmonic nanostructures is joule heating or the process of heating a material by the current flow and the resistance (damping) of the current as it flows through the metallic structure. Heat is localized at the metallic nanostructure and then dispersed into the external media depending on the thermal conductivity of the dielectric media [13,14,29]. The generic equation that describes energy accumulation in a system is,

$$\frac{dE}{dt} = E_{in} - E_{out} + Q + W \tag{22}$$

where E is the energy accumulated in the system, E_{in} is the energy added into the system, E_{out} is the energy removed from the system, Q is the heat generated or consumed by the system, and W is the work added or removed from the system. Typically, with heat transfer in plasmonic materials we are mostly concerned with steady state operation (like when under CW laser irradiance), so temporal dependence of the accumulated energy and therefore temperature increase can be neglected. Due to the lack of mechanical agitation, work applied/generated can also be ignored. When combining the energy balance equation with Fourier's Law of Conduction,

$$q = -\kappa \cdot \nabla \mathrm{T} \tag{23}$$

the heat transfer equation defining the heat generated and transferred due to metallic nanostructures embedded in a solid media simplifies to Poisson's equation,

$$\nabla \cdot [\kappa \nabla T(r)] = -q(r) \tag{24}$$

inside of the nanoparticle and

$$\nabla \cdot [\kappa \nabla T(r)] = 0 \tag{25}$$

outside of the nanoparticle, where negligible attenuation of the incident optical source is assumed for the surrounding media, where κ is the thermal conductivity tensor, ∇T is the spatially dependent temperature gradient, and q(r) is the power density in the metallic nanostructure. The heat input to the nanoparticle is defined by the absorption of the nanoparticle to the incident optical source,

$$Q = C_{abs} I \tag{26}$$

where I is the laser beam irradiance,

$$I = \frac{n_o c_o \varepsilon_o}{2} |E_o|^2 \tag{27}$$

where E_o is the incident electric field of the optical source (i.e. laser beam) [14,28,29]. Figure 17 shows the optical power absorbed in gold and titanium nitride particles on glass substrates at different particle sizes (r=5, 10, and 25 nm) assuming a uniform circular beam 0.5 mm in diameter (poor assumption in general, but utilized for simulation purposes). Power absorption increases with increasing particle size due to increasing absorption cross section (assuming laser incidence is tuned to plasmonic resonance) Gold also has higher power absorption compared to titanium nitride due to the higher absorption cross section which arises from its superior dielectric properties.

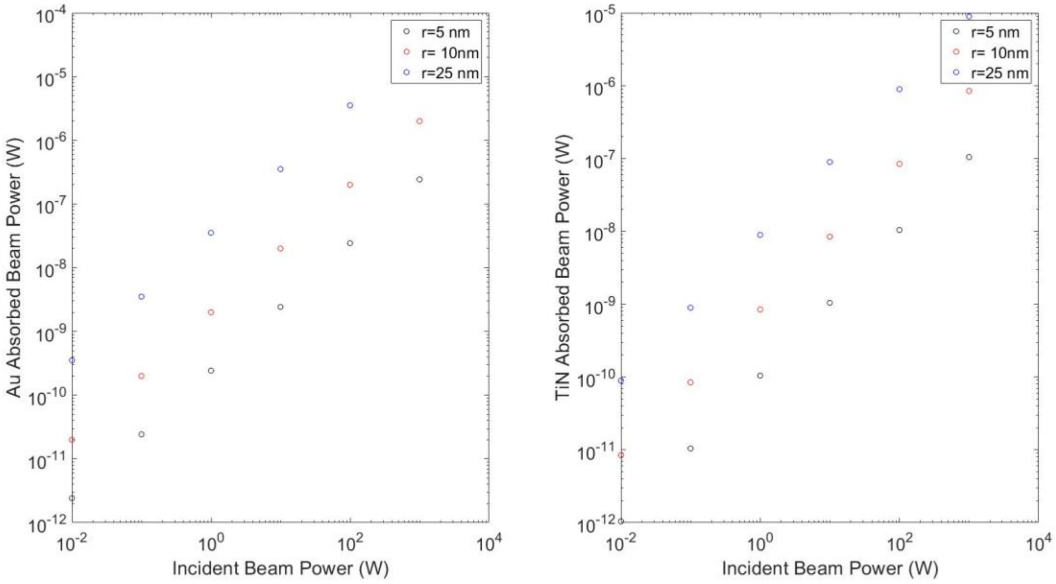

Figure 16. Absorbed laser power for gold and titanium nitride as a function of the input laser power

The heat generated inside the nanoparticle is described by the power density in the metallic nanoparticle,

$$q(r) = \left(\frac{1}{2}\right) Re[J^*(r) \cdot E(r)] \tag{28}$$

where $J^*(r)$ is the complex conjugate of the current density in the oscillating nanoparticle defined by,

$$J(r) = i\omega P = i\omega\varepsilon_o\varepsilon(\omega)E(r) \tag{29}$$

where P is the polarization of the metallic nanostructure under an applied electric field. Using these simplifications, the power density in the metallic nanoparticle can be simplified as

$$q(r) = \left(\frac{\omega}{2}\right) Im(\varepsilon(\omega))\varepsilon_o|E(r)|^2 \tag{30}$$

under the assumption of continuous wave (CW) illumination the temperature change inside and outside of the metallic nanostructures are simplified from Equations 22 and 23,

$$\delta T(r) = \frac{\delta T_{NP} R}{r} \; if \; r > R \; (Outside \; NP) \tag{31}$$

and

$$\delta T(r) = \delta T_{NP} \; if \; r < R \; (Inside \; NP) \tag{32}$$

where

$$\delta T_{NP} = Q/(4\pi \kappa_s R) \tag{33}$$

where r represents radial position, R is the nanoparticle radius, and κ_s is the thermal conductivity of the substrate [13, 14, 28]. Equations 30 and 31 represent the temperature generation from metallic nanoparticles with spherical geometries. Table 2 summarizes some key non-optical properties of gold, silver, and titanium nitride including density, heat capacity, and thermal conductivity as well as optical (refractive index and dielectric function) and non-optical properties for key media (air, water, and glass) relevant to thermoplasmonic research. Utilizing substrate thermal conductivities from this table, and the assumptions utilized for calculating absorption cross sections and absorbed incident power, changes of metallic nanoparticle temperature and its immediate surroundings are calculated and demonstrated in Figure 17. Changes in temperature in the metallic nanoparticles are most significant at high input powers (laser irradiances) at large particle sizes, again due to increased absorption cross sections. Temperature increases in gold nanoparticles are 2-4x higher than those in titanium nitride nanoparticles and changes in nanoparticle temperature as a function of particle size and input laser power can be seen in Table 5 of the Appendix.

Table 2. Relevant properties of significant plasmonic materials (gold, silver, and titanium nitride) and substrates/media (air, water, and glass)

Material	Density (g/cc)	Heat Capacity (J/mol K)	Thermal Conductivity (W/mK)	Refractive Index	Dielectric Constant
Gold	19.3	25.4	318	X	X
Silver	10.5	25.4	429	X	X
Titanium Nitride	5.21	24	29	X	X
Air	0.00132	29	0.026	1	1
Water	1.00	75.4	0.60	1.33	1.77
Glass	2.2	45.3	1.3	1.5	2.25

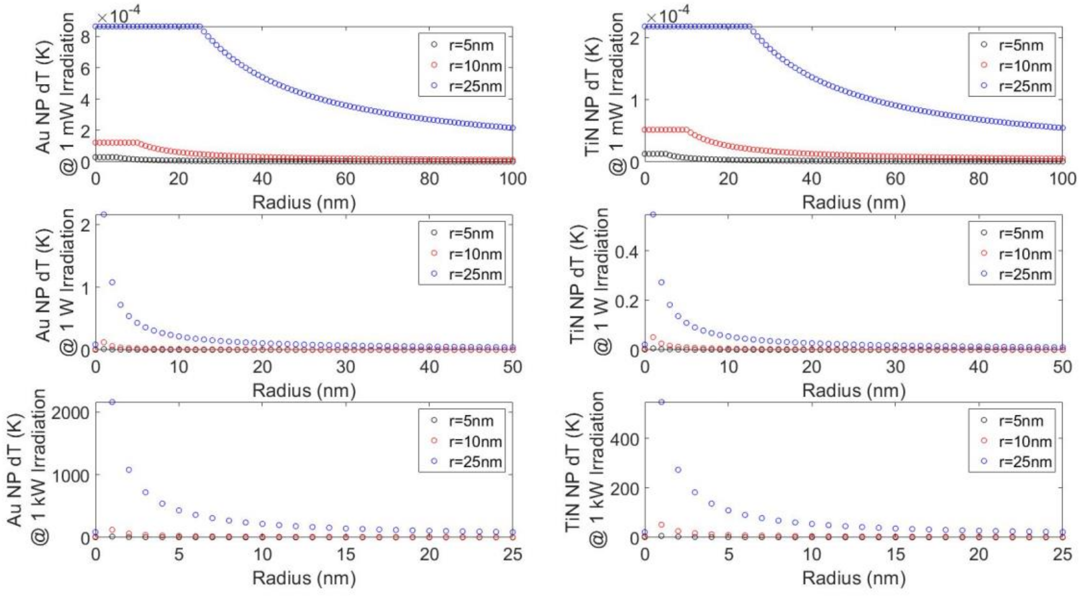

Figure 17. Radial temperature change profiles in gold (left) and titanium nitride (right) at different NP sizes and incident laser powers (top-bottom, 10mW, 1 W, 1kW).

Mathematical descriptions for other nanostructured geometries are quite involved, but a simplification often assumed is,

$$\delta T_{NP} = Q/(4\pi\beta\kappa_s R_{eq}) \tag{34}$$

where R_{eq} is an equivalent radius based off the nanostructures characteristic length and β is a correction factor for material geometry. Finally, it is important to note that metallic nanostructures are quick to reach thermal equilibrium with the transient time for heat diffusion into the surrounding media being described as,

$$\tau_{tr} \sim L^2 \rho c_p / 3\kappa_s \tag{35}$$

where L is the characteristic length (i.e. diameter for spheres), ρ is the nanomaterial density, and c_p is the metallic nanostructure heat capacity[14]. Figure 18 shows the transient, steady state diffusion times, calculated from the values tabulated in Table 2, from the metallic nanostructure to its environment for gold, silver, and titanium nitride as a function of the characteristic particle size (diameter) and substrate. As demonstrated by the figure, increasing the characteristic size of the particle increases the time required for thermal equilibrium due to the longer heat transfer length scales. Heat transfer times also get longer as a function of the thermal conductivity of the substrate; heat transfer in glass is faster than heat transfer in water which is faster than heat transfer in air due to decreasing thermal conductivity of the respective media. The thermal transient time for the glass is so low it rides along the x-axis in Figure 19. Transient heating times for silver, gold, and titanium nitride are demonstrated in Table 6 in the Appendix.

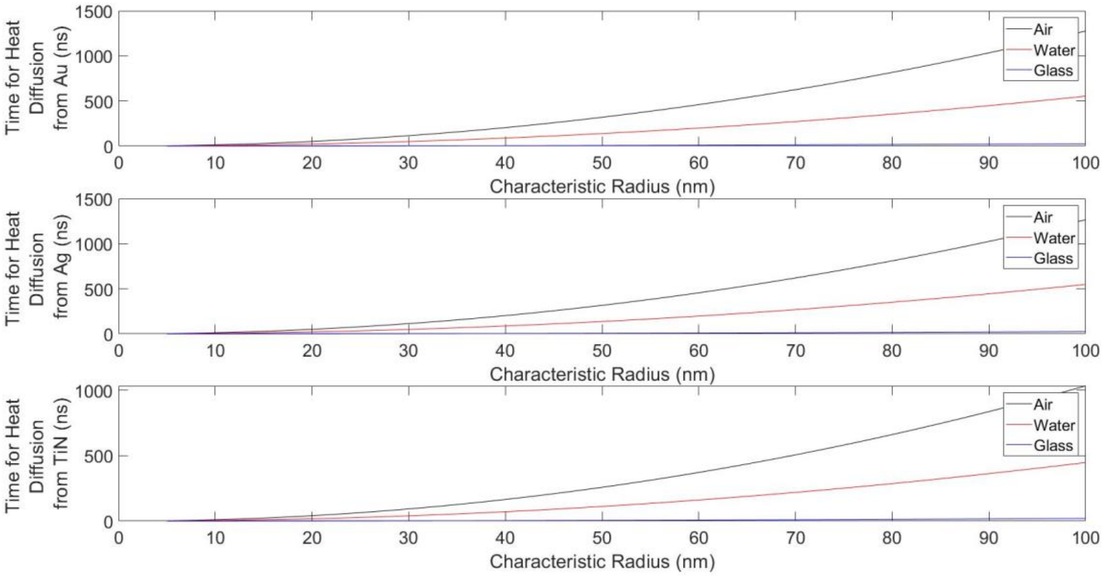

Figure 18. Transient heat transfer times for metallic nanostructures (Top-Bottom, Au, Ag, and TiN) for different characteristic radii and substrates (air, water, and glass)

Another interesting thermal system are metallic nanostructures under femtosecond and nanosecond pulsed laser illumination. The modelling and theory for pulsed laser heating is more complicated because steady state assumptions do not typically apply. Absorption of metallic nanostructures are described by three steps. In the first step, energy is absorbed by the free electrons from the incident pulsed laser source, without transferring energy in the lattice (resistive heating). In the second step the electrons cool down and transfer energy into the metallic lattice in the form of phonons, in which the electrons and the ionic nucleus reach a thermal equilibrium. The third and final step is heat diffusion through the external environment which acts to cool the metallic nanostructures. The timescales for pulsed laser heating and phonon generation in the metallic nanostructures are much faster than the heat diffusion out of the metallic nanostructure in the surrounding environment. The mathematics and models change drastically depending on the timescales and frequency of the laser pulses relative to phonon generation and thermal diffusivity

[14]. This report does not investigate in detail heat transfer modeling with different pulsed laser heating configurations.

3.2 Measuring Temperature with Plasmonic Nanostructures

While modeling and estimating the temperature distributions in metallic nanostructures and their surrounding media can be challenging, measuring the temperatures of metallic nanostructures can be equally problematic due to their confined dimensions. Temperature measurements utilized to probe the temperature of the bulk, like thermocouples and thermometers, cannot accurately probe the temperature of the metallic nanostructure, where interesting processes for thermoplasmonics typically occur. Four methods developed to probe changes in temperature from metallic nanostructures include: scanning thermal microscopy, surface enhanced Raman spectroscopy, fluorescence polarization anisotropy spectroscopy, and quadriwave shearing interferometry. Scanning thermal microscopy is a variation of atomic force microscopy, where an ultra-fine oscillating probe tip raster's across a surface and produces images based off changes in laser deflection on the backside of the oscillating cantilever, allowing for sub-diffraction limit imaging. When operated in temperature contrast mode, a resistive thermocouple element is built into the probe tip using lithographic methods and is connected to a Wheatstone bridge circuit. The resistance of the probe changes with temperature during the raster of the surface, which is measured through the Wheatstone bridge's adjustment to maintain voltage, allowing for spatial temperature maps of the surface. A schematic for this experimental set-up is shown in Figure 19 where the probe tip rasters across the surface of a sample, typically over a fairly small area (up to a couple of square microns), and changes in laser deflection are recorded on a spatially sensitive photo-diode in order to generate a topography map. The tip is also designed as a thermocouple probe, typically formed through microfabrication methods and is connected to the Wheatstone bridge to generate a thermal distribution topography map. The bottom of the figure shows both the topological as well as the thermal map of the surface structure. The limitation of this technique is that is can only probe the sample surface, heat transfer transients can exist between the probe tip and sample, and data acquisition and analysis can take a long time [29].

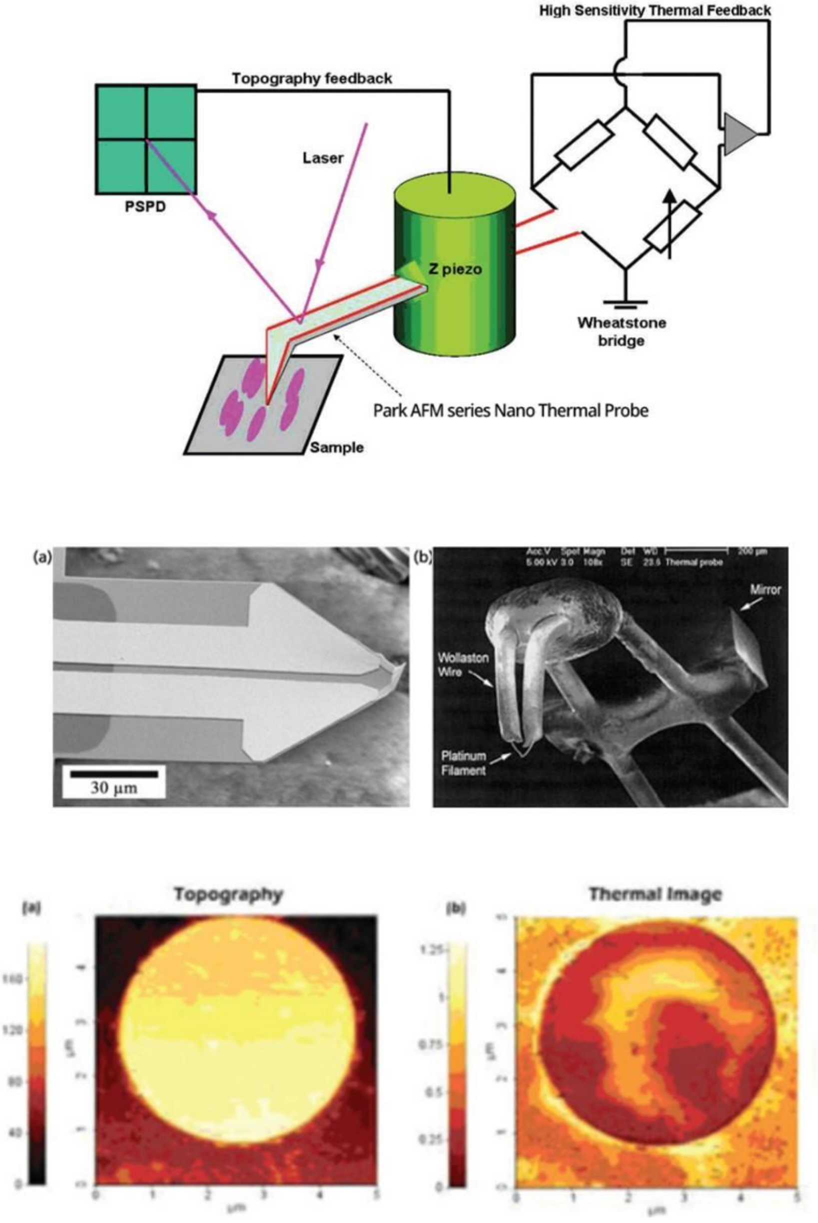

Figure 19. Top. schematic of scanning thermal microscopy configuration. Middle. Specialized scanning probe tip functionalized as a resistive thermocouple. Bottom. Scanning probe image of both surface topography and thermal map [29]

Another technique useful for probing temperature changes in metallic nanostructures directly is surface enhanced Raman spectroscopy (SERS). Raman spectroscopy is an optical scattering technique utilized to study chemical bonding states in materials by measuring shifts in the frequency (momentum) of an incident optical beam (Raman Shift) due to momentum transfer from the chemical bonds or phonon distributions intrinsic to the incident material. Stokes scattering results in a Raman shift from emission of phonon's into the incident material (red shift) and anti-Stokes scattering results in a Raman shift from absorption of phonon's from the chemical bonds into the incident optical beam (blue shift). Raman spectroscopy is extremely sensitive to bonds that are highly polarizable (like double and triple bonds. [2,3] In SERS, an organic molecule with a particular functional group (for example, C≡N) with a characteristic Raman shift is grafted/adsorbed onto the surface of the metallic nanostructure. Temperature changes due to heating from incident laser radiation are measured through the changes in the Raman shift frequency or changes in the full width half maximum, (FWHM-i.e. bandwidth) though the frequency position is more popular due to convenience in measuring. Raman is sensitive the molecular bonds that are polarizable such as π bonds in double or triple bonded organic materials and the phonon distribution within a crystalline material. When a material is heated the lattice expands or the polarization of the bond lengths increases which causes an increase in the phonon lengths in the material and consequently a change in the position of the corresponding shift. A single beam can be utilized to both induce a plasmonic response and a Raman shift in the functionalized nanostructures. The drawbacks of SERs include damage of bound ligands during intense laser irradiation (and therefore reduction in Raman signal) which reduces the maximum operating temperature of the technique, diffraction limitations for surface mapping, and necessity of utilizing chemical functionalities to measure temperature which may not be required or desired for end-product use [30].

A demonstration of utilizing SERS to measure changes in temperature can be seen in Figure 20. In this work gold nanoparticles were developed using seed mediated techniques (chemical reduction from salts) and deposited onto a glass slide. They were functionalized with phenyl isocyanide (PIC) by soaking in an ethanol/PIC solution, to detect the Raman shift from the C≡N bond in PIC. In this work a 633 nm laser is utilized as both the excitation laser for the nanoparticle heating and for observing the Raman shift. It is clear in this case that increasing temperature from increasing input laser power results in a red shift of the Raman peak and a broadening of the full width half maximum up to 100^{o}C. Above this temperature the Raman signal begins to fade away, most likely due to destruction or desorption of the PIC grafted onto the gold particles. From this data it is observed that the shift has a stronger linear relationship to temperature than the FWHM, and because it is simpler to measure, it is typically utilized for temperature measurements. Figure 21 shows both a white light image of cell cultures and Raman-induced temperature map of a culture of CaSki cells utilizing the Raman shift. Temperature mapping utilizing SERS shows the ability to identify temperature differences in aqueous medium with and without the cell cultures. [30]

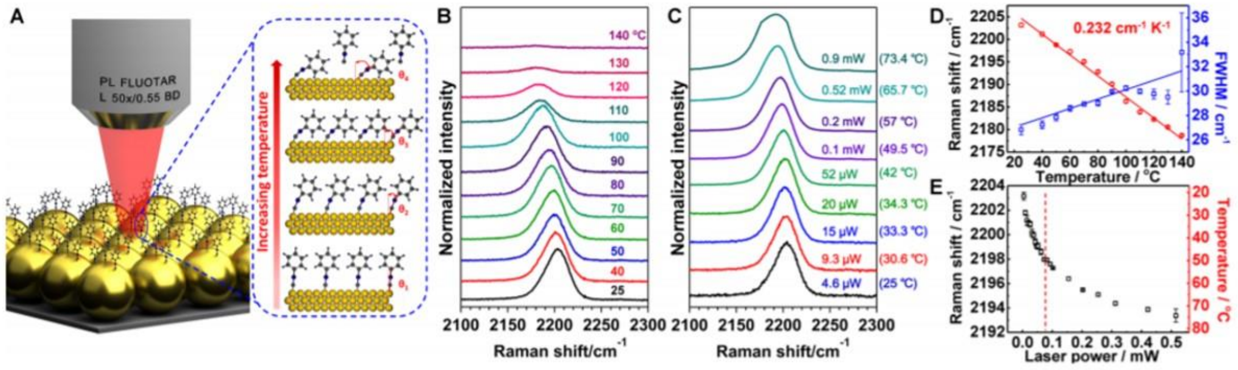

Figure 20. Utilizing SERS to measure the temperature of gold nanoparticles under laser Illumination using the Raman shift [30]

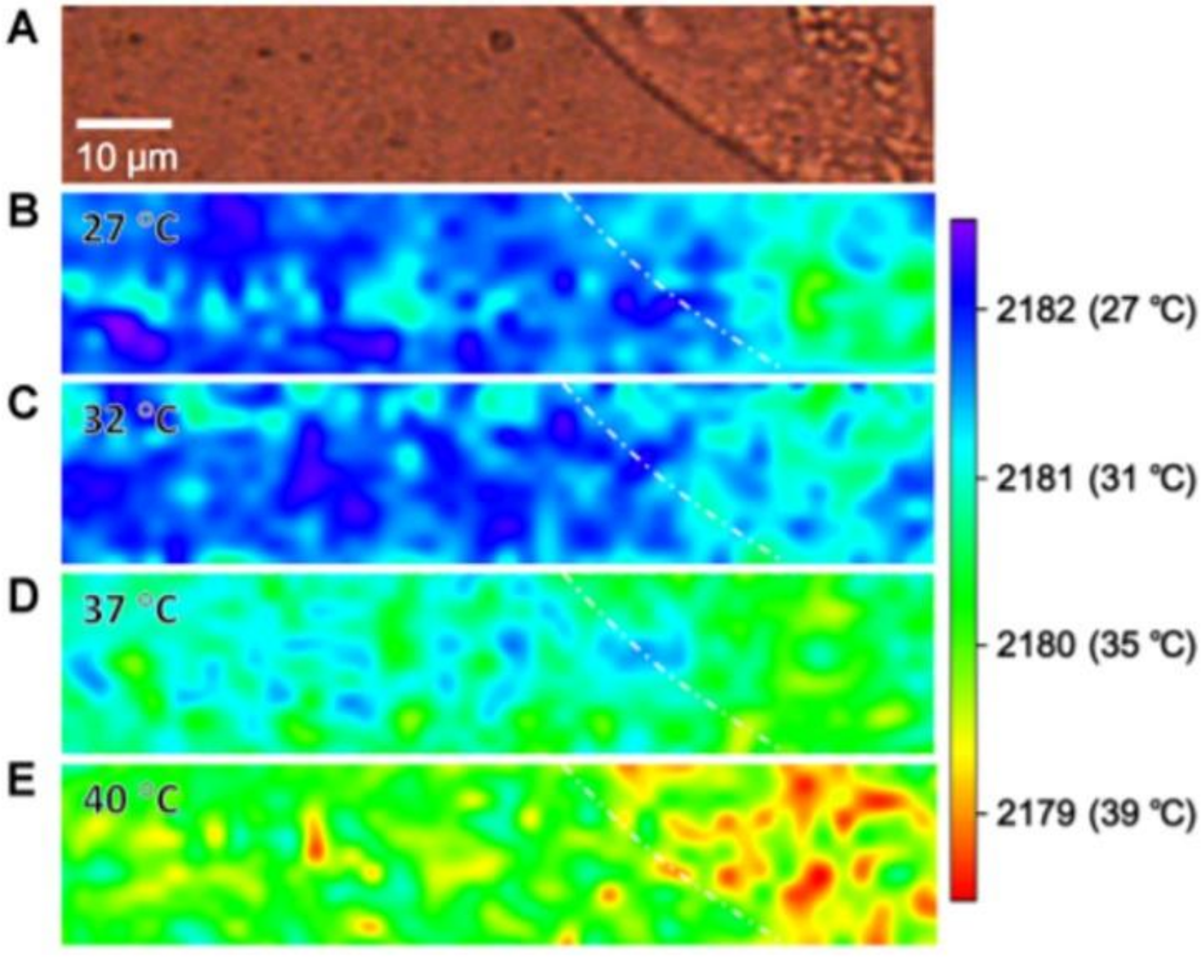

Figure 21. Temperature map generated utilizing SERS [30]

Another optical analytical technique for probing temperature distributions of metallic nanostructures and their media is fluorescence polarization anisotropy spectroscopy, a technique that measures intensities of fluorescence at different polarizations for a molecule under Brownian dynamics (molecule flow/mobility in a fluid). In this technique metallic nanostructures are functionalized (similar to SERS) with a fluorescent marker material in fluid with a (preferably) strongly temperature dependent viscosity. When in random Brownian motion, a fluorescent molecule emits light at polarizations and intensities depending on the molecule's position that are defined by a particular polarization anisotropy. The polarization anisotropy is related to the fluorescence lifetime and a rotational correlation time for the molecule which is related to the temperature dependent solution viscosity and therefore temperature of the molecule. By measuring the intensities of both the parallel and perpendicular polarized components of the fluoresced light, relative to the initial polarization of the laser source, the temperature can be extrapolated. In this experimental set up, two laser beams are utilized, a CW laser tuned to the resonant absorption peak of the plasmonic nanostructure array/film to heat the plasmonic structures (typically an NIR or visible laser) and a linearly polarized laser to induce fluorescence of the adsorbed fluorescent molecule (typically a high photon energy laser in the UV or deep blue light range). [31]

Figure 23 shows an example of the experimental set up and temperature mapping utilizing fluorescence polarization anisotropy spectroscopy. In this set up a Ti:Sapphire NIR laser is utilized to induce plasmonic oscillations in gold nanostructures (lithographic structures or colloidal nanowires) functionalized with fluorescein (a photostable and high quantum efficiency xanthene chromophore) and a linearly polarized 473 nm beam is utilized to induce fluorescence in the fluorescein marker. Fluoresced photons of different polarizations are separated with a polarizing beam splitter cube and measured on separate avalanche photodiodes. Both beams are focused down through a microscope objective and scanned across the surface for measurement and the polarization anisotropy is pre-calibrated against a temperature change using standard thermocouples. The images generated in the figure show the standard optical image of colloidal gold nanorods on a glass slide, the fluorescence polarization anisotropy spatial map, and temperature map generated by correlating the polarization anisotropy to the temperature and temperature dependent viscosity around the gold nanostructures [31].

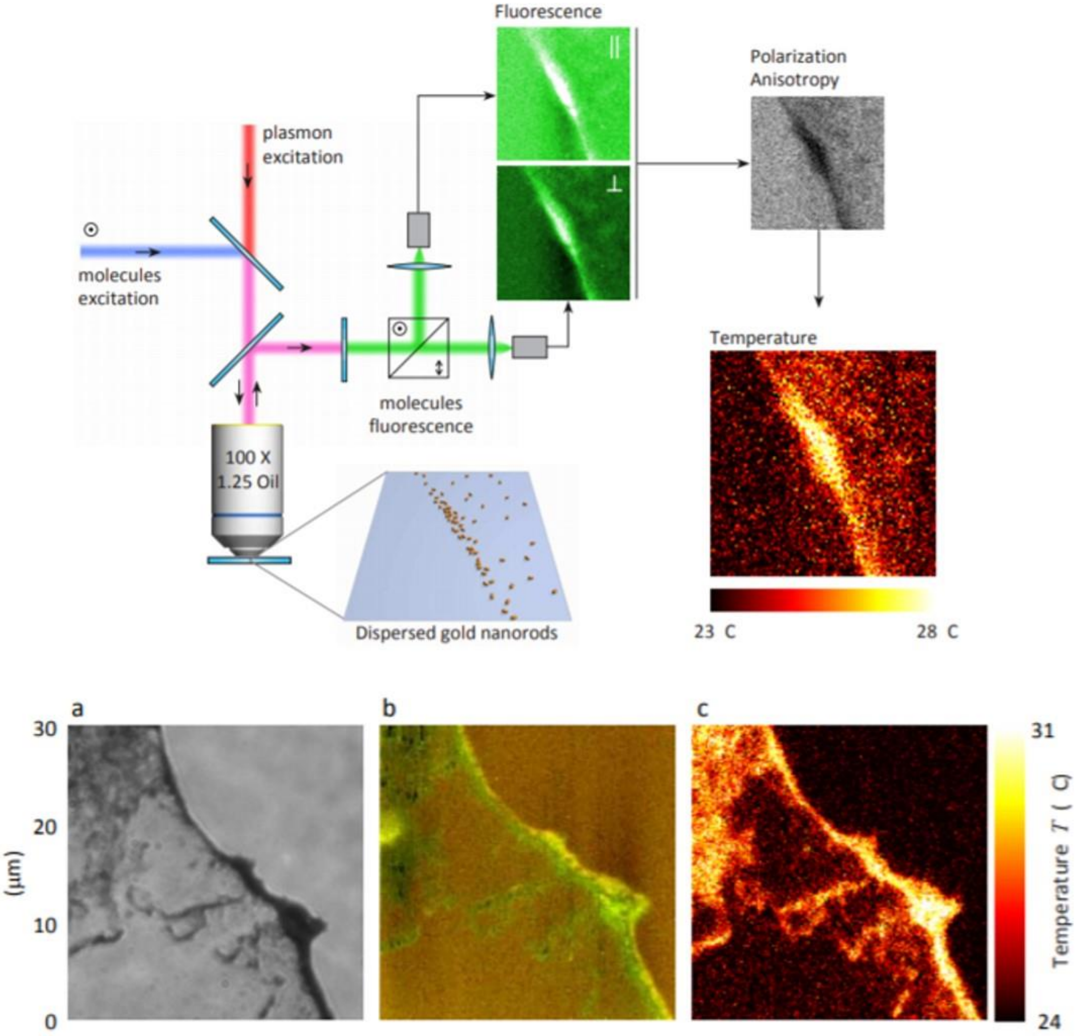

Figure 22. Fluorescence anisotropy microscopy [31]

The final methodology to be discussed in this report for imaging plasmonic structures is quadriwave shearing interferometry, a technique which measures temperature induced changes in the refractive index in the media around plasmonic nanostructures. The technique utilizes a modified Hartman grating and a CCD detector for the wavefront analyzer and can be modified from any traditional white light microscope in transmission mode. An example of this configuration can be seen in Figure 24, where the sample is illuminated under a Köhler configuration and utilizes a numerical aperture to improve spatial coherence. A separate laser is utilized to heat the plasmonic nanostructures at a frequency tuned to their resonance (typically at 532 nm or 808 nm) which is focused onto the objective pupil with the beam diameter controlled by a separate diaphragm for uniform illumination. The sample is then imaged onto the CCD detector with the modified Hartman grating. With this methodology, the optical path difference (OPD), is calculated by analyzing wavefronts before and after heating, where the OPD is caused by temperature induced changes in refractive index of the media surrounding the metallic nanostructure. The right side of the figure shows the spatial temperature map of the OPD, the heat power density, and the change in temperature for a 300 nm diameter, 20 nm thick gold “cylinder” on glass, surrounded by water, under variable laser irradiation. The spatial resolution of the imaging is diffraction limited by λ/NA, but this technique can detect temperature changes on the order of 1 K. It is a fast technique that does not require raster of a laser across the sample. It also does not require sample modification in order to make it sensitive to measurement (i.e. fluorescent markers or Raman-active species). Finally, in addition to temperature mapping, it can be utilized to measure heat source density and absorption cross sections [18].

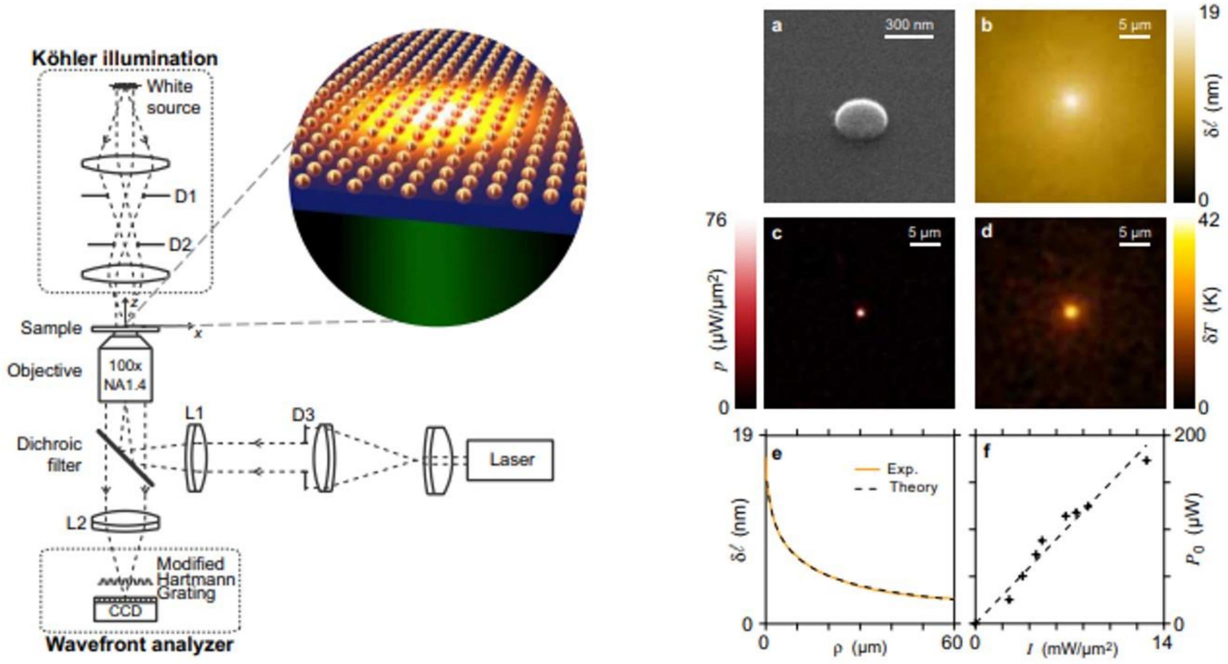

Figure 23. Quadriwave shearing interferometry for analyzing nanostructure temperature [18]

4 Applications of Thermoplasmonics

4.1 Biomedical Applications

Historically, the biomedical field has dominated the application space for plasmonic materials primarily for sensing applications. Currently the biomedical field is investigating plasmonic nanostructures for uses in photothermal therapy and nano-surgery. In this application, plasmonic nanostructures are used to selectively induce apoptosis in carcinogenic cells through hyperthermia, or excessive heating of the cells through heating of the structures under optical irradiation from a laser beam. By tuning the shape of metallic nanostructures, for example through the synthesis of core/shell dielectric/metal structures, the optical resonances frequency can be shifted to the near infrared region, where cellular tissue is typically transparent, allowing for focused damage on carcinogenic cells instead of healthy cells. Destruction mechanisms of cells functionalized with metallic nanostructures include thermal damage in the case of CW laser illumination and bubble formation in the case of pulsed laser illumination. In the case of thermal degradation, cells can either be destroyed due to thermal denaturation of proteins of destruction of particular molecules utilizing hot, free-electrons generated during the plasmon oscillation process (i.e. plasma damage). Another potential application in the biomedical field is drug delivery, where pulsed laser irradiation of metallic nanostructures generate bubbles around the structure which can be utilized to break the liposome membrane to release its contents, which can be used to increase the rate of the drug release process [32].

4.2 Chemical Applications

Another application of thermoplasmonics is in the chemical industry utilizing plasmonic nanostructures for enhancing chemical reaction rates. Chemical reaction rates are typically described, as a function of temperature, by the Arrhenius Equation,

$$k = k_o \exp\left(\frac{-E_a}{RT}\right) \tag{35}$$

Where k_o is a pre-exponential factor, E_a is the activation energy, and R is the ideal gas constant. Upon illumination, plasmonic nanostructures vibrate and heat up, increasing the temperature of the metallic structures which can also lead to heating of the host media, increasing the reaction coefficient and therefore the reaction rates. Typically, materials used for plasmonic nanostructures, like gold and platinum (though gold is better from a plasmonic efficiency standpoint) also have enhanced catalytic characteristics, and the nano-scale dimensions allow for materials with high surface area to volume ratios, allowing for a higher degree of reactivity due to an increased number of reactive sites on the surfaces of the metallic nanostructures [33-34].

Plasmonic nanostructures also contribute to increased catalysis through a process called “hot electron chemistry,” where hot electrons generated by the plasmonic oscillation contribute to the chemical reaction. These electrons can either contribute directly in the chemical reaction or can be injected into the conduction band of another material to form reactive species on the surface of the support material for contributing to chemical reactions. In the former process hot electrons are highly reactive and can be utilized in redox reactions (reactions based on electron charge transfer). An example of this would be in free radical polymerization where the hot electron can be utilized to break the vinyl (carbon-carbon double bond) in an organic monomer to initiate free radical polymerization. By patterning metallic nanostructure, polymers with unique nanostructures can be developed [35]. In the latter reaction process, metallic nanostructures can be deposited on semiconducting materials with intermediate bandgaps (like TiO_2). When irradiated, the excited conduction electrons from the metallic nanostructures are injected into the conduction band of the semiconducting materials and are used to form reactive free radical species on the surface of the semiconductor. (oxides, hydroxides, peroxides) These reactive species can be utilized to increase the reaction rate of several reaction mechanisms including oxidation and water splitting reactions. This only works with materials with moderate bandgap width, like TiO_2 (~3 eV). If the bandgap is too low the semiconductor transition can be directly driven by the incident laser irradiation and if it is too high the electrons do not have enough energy to be injected into the conduction band, like Al_2O_3 (bandgap>6 eV) [33].

Figure 25 shows an example of how metallic gold structures deposited on titania and alumina particles can be utilized under laser irradiation to support the catalytic oxidation of glycerol into glyceric and tartronic acid products (as well as some other acidic reaction byproducts). In this case gold NP's loaded on titania and alumina substrates were acquired directly from a commercial vendor. Data from the figure shows that the when the catalysts are loaded with gold nanoparticles the steady state temperature increases to 60^{o}C for both titania and alumina supports at the highest laser irradiance (2.25 W with a 532 nm laser diode) compared to just under

30^{o}C for non-gold functionalized catalysts at the same laser irradiation. The figure also shows the conversion efficiencies under a variety of thermalization conditions. Catalyst free and room temperature show zero or near zero conversion and serve as the reference case. Laser activation (2.25 W) of the gold/titania and gold/alumina reach nearly 90% and 50% respectively with thermal activation of the same processes reaching only about 40% for both cases. As seen with both cases laser-induced catalysis can improve conversion efficiencies of chemical processes (in this case glycerol oxidation) by increasing the temperature of the metallic nanoparticles at the location of the catalyst. The gold/titania catalyst exhibits a much more significant increase in catalytic efficiency due to the use of hot electron chemistry where energized electrons are injected into the conduction band in the TiO_2 catalyst and are utilized to generate free radical compound which contribute to the catalytic reaction process. A schematic of the process for hot electron chemistry is also demonstrated in Figure 25 [33].

Another chemical process which Thermoplasmonics is supporting is in the field of selective distillation, where the metallic/semiconductor nanostructures are used to help with chemical separation processes. Utilizing metallic nanostructure hotspots in chemical mixtures under optical irradiation allows for increased heating of the mixture, allowing for separation based off the material boiling points. By utilizing these structures with broad band absorption tuned to the solar spectra in concentrating solar plant configurations chemical separation plants with reduced environmental impact can be established [36].

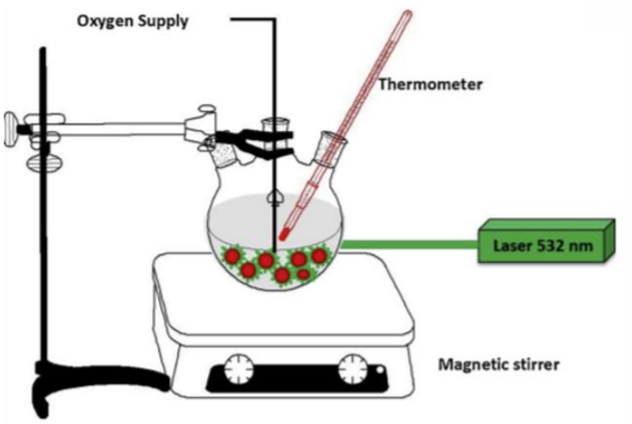

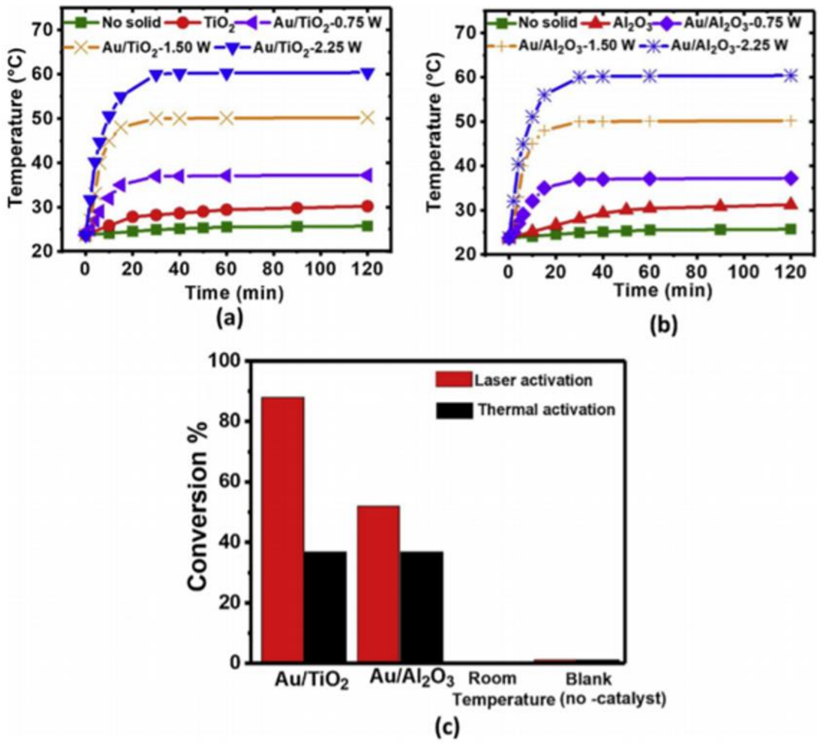

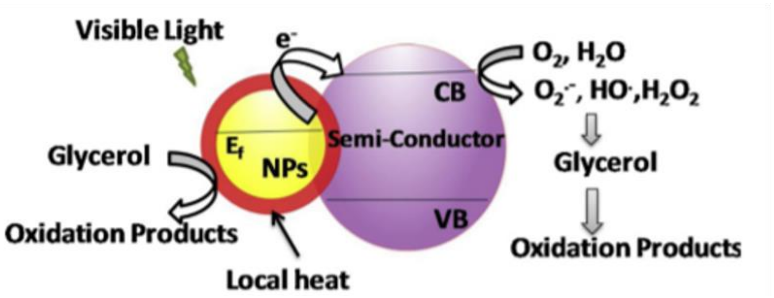

Figure 24. Thermoplasmonic enhancement of catalytic chemical processes [34]

3.2 Solar Desalination Applications

Due to the capabilities of these nanostructures to generate high amounts of heat locally, they are being investigated in desalination process for enhancing water evaporation, particularly in membrane distillation processes. Membrane distillation, a rival desalination technique to reverse osmosis, utilizes a hydrophobic, porous (usually microporous) membrane to separate salts from either sea or brackish water utilizing a temperature gradient between the front and back side of the membrane. Feed water on one side of the membrane is heated, ideally with a concentrating solar source for commercial applications, forming a vapor at the membrane interface that flows to the other side of the membrane and condenses, leaving behind the ionic components. This method requires low energy input and can reach high conversion efficiencies compared to reverse osmosis due to avoiding the limitations regarding osmotic pressures. By embedding metallic nanostructures, such as silver nanoparticles in the microporous membranes, higher temperature fluxes at the membrane interface can be achieved, which can improve vaporization rates and therefore clean water recovery. This helps to overcome problems due to "temperature polarization," the phenomena where the latent heat removed at the interface causes the temperature at the membrane to be lower than the bulk [37-38].

An experimental set-up to demonstrate plasmonic-enhanced membrane desalination can be seen in Figure 26. In this experiment, silver nanoparticles synthesized through the chemical reduction method from a silver salt solution are mixed with PVDF homopolymer in solution to form a microporous membrane through a phase inversion process. The membrane is installed into an apparatus with a feed water supply delivered on one side of the membrane, a distillate outlet on the other side of the membrane, and a quartz window to allow for irradiation of the membrane with a mercury lamp. As seen in the figure, increasing the concentration of silver nanoparticles increases the absorption of the solution, with plasmonic resonances tuned to the ultra-violet to the deep blue range. With the increased concentration in silver nanoparticles an increase in the temperature of the bulk solution is observed. Finally, the figure shows the difference in water vapor flux across the membrane for both pure water (left) and water loaded with a 0.5 M concentration of NaCl. Loading of the membrane with silver nanoparticles for both cases increase the water flux across the membrane by a factor of nine for the pure water and eleven for the case of the saline solution, compared to the case of the unloaded membrane, indicating enhanced heating and vaporization due to the presence of the densely loaded plasmonic nanostructures. [37]

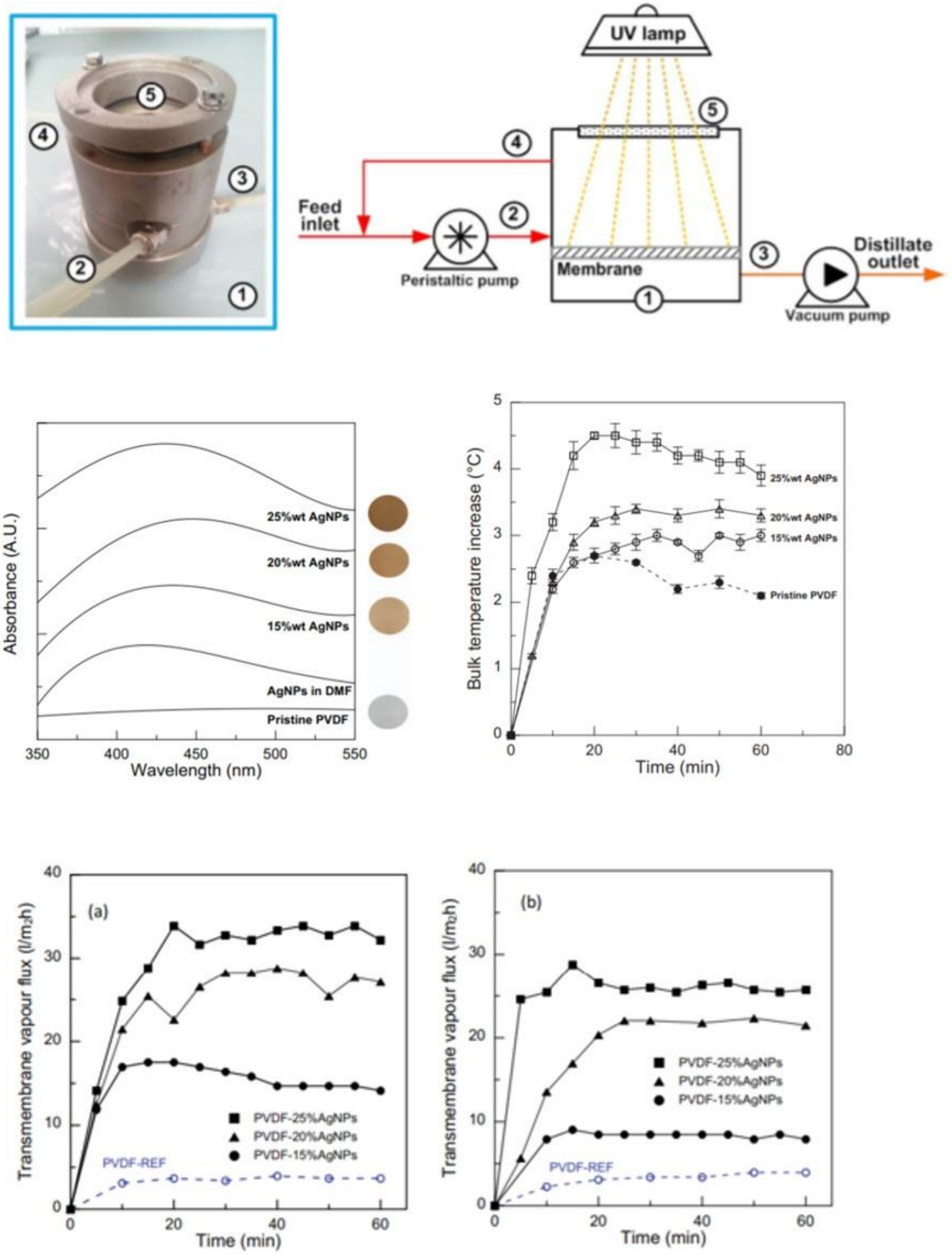

Figure 25. Thermoplasmonics enhanced heating for desalination [37]

3.3 Thermophotovoltaic Applications

Plasmonic nanomaterials are also being investigated for developing thermo-photovoltaic systems capable of beating the traditional blackbody efficiency limits. In these architectures a thin metallic film, which serves as an emitter, is placed in front of a thin film semiconductor and separated by a vacuum gap. The emitting plasmonic layer is a high band gap material and operates at a high temperature (up to 1200 K) where the black body emission spectrum is tuned to the bandgap of the semiconductor material (1-2 μm or <1 eV) operating near room temperature (300K). Because the emission spectrum of the plasmonic thin film is tuned directly to the semiconductor bandgap, there are fewer thermal losses due to high energy photon absorption and zero absorption of photons below the semiconductor bandgap energy. Thermophotovoltaic systems either operate in the far field where energy transfer is dominated by radiative transfer through air or in the near field where the separation between the emitter and the photovoltaic unit is small so evanescent waves can be coupled into the solar cell to increase energy transfer. Materials like indium-doped tin oxide and graphene have been investigated as plasmonic emitters because of their strong plasmonic response in the near infrared. Semiconductor materials like GaSb (0.7 eV), InAs (0.36 eV, InGaAs, and InSb (0.17 eV) due to their low bandgaps are considered for the PV cell material. The thinner the gap between the emitter and semiconductor can be made, the more efficient and higher power density device can be designed due to increased efficiency in radiative and evanescent energy transfer . Using this method thermo-photovoltaic cells of 40-60% efficiency have been theoretically designed for high temperature emitter/semiconductor tandems. Nanostructured metallic refractory materials, such as tungsten or titanium nitride, can also be developed as broadband solar absorbers for concentrating solar applications like concentrating solar power or chemical plants where the material must be stable to a high solar flux. In these applications, traditional plasmonic materials like silver and gold cannot be used due to melting at elevated temperatures [20-21].

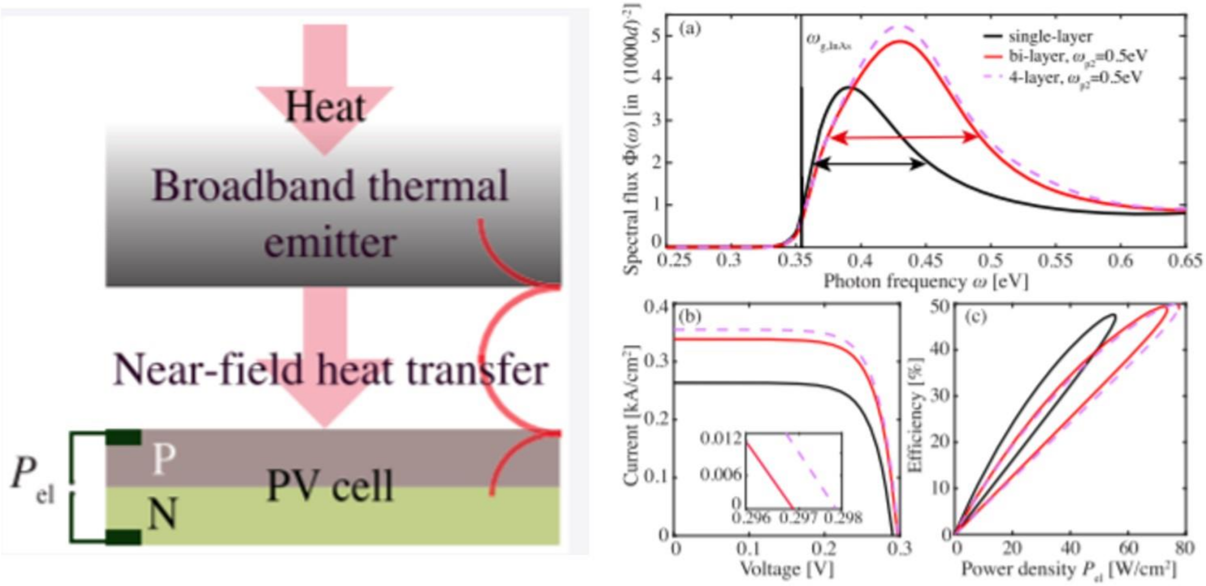

Figure 26. Thermoplasmonic solar cell design [20]

Figure 27 shows the schematic for a thermo-photovoltaic solar cell configuration where a broad-band thermal photon emitter is separated from a solar cell by a vacuum gap and has its blackbody emission spectrum tuned to the bandgap of the semiconductor. In this work the authors provided a theoretical framework for a thermophotovoltaic system with a broadened emission to account for nonradiative recombination and improve efficiency by increasing the theoretical open circuit voltage and short circuit current. Several designs for spectral emission flux are also demonstrated in the figure utilizing an ITO emitter and an InAs solar cell, including single layer, bi-layer, and 4 layer emitter designs. Increasing the number of layers serves to increase the bandwidth of the emission spectrum, as demonstrated by Figure 27. By tuning the deposition conditions and chemistry of ITO the plasmon frequency and therefore the emission frequency of the ITO film can be tuned (increasing the plasmon frequency blueshifts the emission spectrum).

With the increased number of emitter layers the spectrum broadens and the amplitude increases, resulting in an increase of the short circuit current density and open circuit voltage for the solar cell and solar cell efficiencies theoretically approaching 50% electrical power conversion can be demonstrated with these plasmonic broadening designs [20].

3.4 Photoacoustic Imaging Applications

Due to the sharpness of the heating gradients in plasmonic nanostructures, thermoplasmonic materials can be utilized for several imaging techniques. The most common were discussed previously, where techniques like SERS or fluorescent anisotropy polarization spectroscopy can be used to measure and image materials by observing temperature gradients from irradiated plasmonic nanostructures. One of the most common applications for plasmonic structures is for imaging cell cultures for biomedical applications like nano surgery and photothermal therapy treatments. Photoacoustic imaging is another technique developed utilizing plasmonic nanostructures that combines optical and acoustic techniques to image materials, most commonly cell cultures. The technique combines the high contrast capabilities of optical imaging with the scatter resistance of acoustics, allowing for deeper penetration imaging into biological samples. This technique couples with thermoplasmonics where metallic nanostructures embedded into a biological sample are irradiated with a laser beam and generate localized heat increases. Through thermoelastic expansion of the nanoparticles and cells, temperature changes generate pressure transients in the sample which can be detected by acoustic techniques. Figure 28 shows a schematic for photoacoustic imaging where absorption of a gold nanostructure from an incident laser beam generates an acoustic wave through thermoelastic expansion which propagates through a solvent and can be detected by acoustic methods. The figure shows that increasing the laser fluence on the gold nanostructures increases the generated photoacoustic amplitude detected by increasing the plasmonic response and thus the pressure transient amplitude. Tuned gold structures with higher absorption to the incident laser wavelength also increase the photoacoustic response [17].

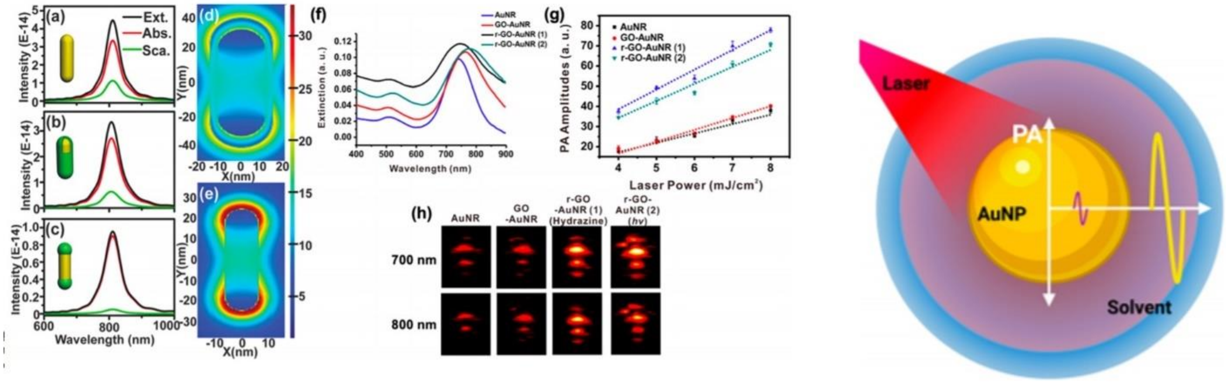

Figure 27. Thermoplasmonic-enhanced photoacoustic imaging [17]

4.6 Defense Applications

A final application of thermoplasmonics is in the defense industry, utilizing metallic nanostructures for initiating insensitive high explosives. Typically, insensitive high explosives (IHE’s) are initiated utilizing primary explosives like lead azide, which are much more sensitive to inputs (impact, friction, shock, etc) and have toxic components. Optical initiation of IHE’s has been studied as safer and environmentally friendly means of initiating explosives. IHE’s typically have strong absorption in the ultra-violet range, weak absorption in the visible range, and virtually no absorption in the near infrared range, where many efficient, high power laser systems operate. Due to this low absorption, high optical powers are typically required to effectively initiate high explosives. In order to avoid the use of costly and bulky UV lasers, metallic nanostructures have been investigated as optical sensitizers at frequencies in the visible and infrared range, enabling the use of much lower cost and easily accessible laser diodes. Both surface coatings of metallic nanostructures on HE crystals and metallic nanostructures embedded into the HE crystals have been studied for enhancing optical initiation of HE’s, though embedding the metallic nanostructures has been demonstrated to be more efficient due to increasing the heating distribution, and therefore bulk temperature, throughout the entirety of the HE crystal. Utilizing metallic nanostructures, such as gold nanoparticles, generates absorption resonances in the visible and near infrared range allowing for initiation with diode lasers, decreased optical power requirements for initiating the IHE’s, and decreased delay time between laser incidence and HE initiation [16,39,40].

Figure 29 shows the application of different plasmonic nanostructures (circles, triangles, and cracked triangles) to aid in the initiation of the insensitive explosive cyclotrimethylene trinitramine (RDX). In this case silver metallic nanostructures are synthesized by seed mediated growth utilizing reduction of aqueous silver salt solutions. The metallic nanostructures were spread on top of RDX and B/KNO_3 cylinders and were irradiated using an 808 nm laser diode. As seen in the figure, utilizing metallic nanostructures reduces both the required input initiation energy and delay time from laser incidence to initiation for RDX and B/KNO_3. For pure RDX, round nanoplates, triangular nanoplates, and cracked triangular nanoplates the initiation energies for detonation decrease from 240 W to 200 W to 180 W, and 100 W respectively. In plasmonic structures, electric field enhancement, and therefore resonance intensity, is a function of the dipole moments. Therefore the more directions a metallic structure can be polarized increases the electric field enhancement. Structures with more edges and points see more enhancement along the edges, which explains why cracked triangular plates outperform triangle plates which outperform round plates. Similarly for the B/KNO_3 the pure, cracked triangular plates, triangle plates, and round plates show a decrease in initiation time from 59.8 ms, 46.8 ms, 36.6 ms, and 29.3 ms respectively. This shows that metallic nanostructures can be utilized to reduce thresholds for laser initiation and decrease initiation delay times for insensitive high explosives. Keep in mind this technique also opens the door for the use of optical initiation of explosives using inexpensive laser diodes in the visible/NIR range (such as 532 nm and 808 nm), by tuning absorption resonances to this range, avoiding the need for expensive (and more hazardous) UV lasers [16].

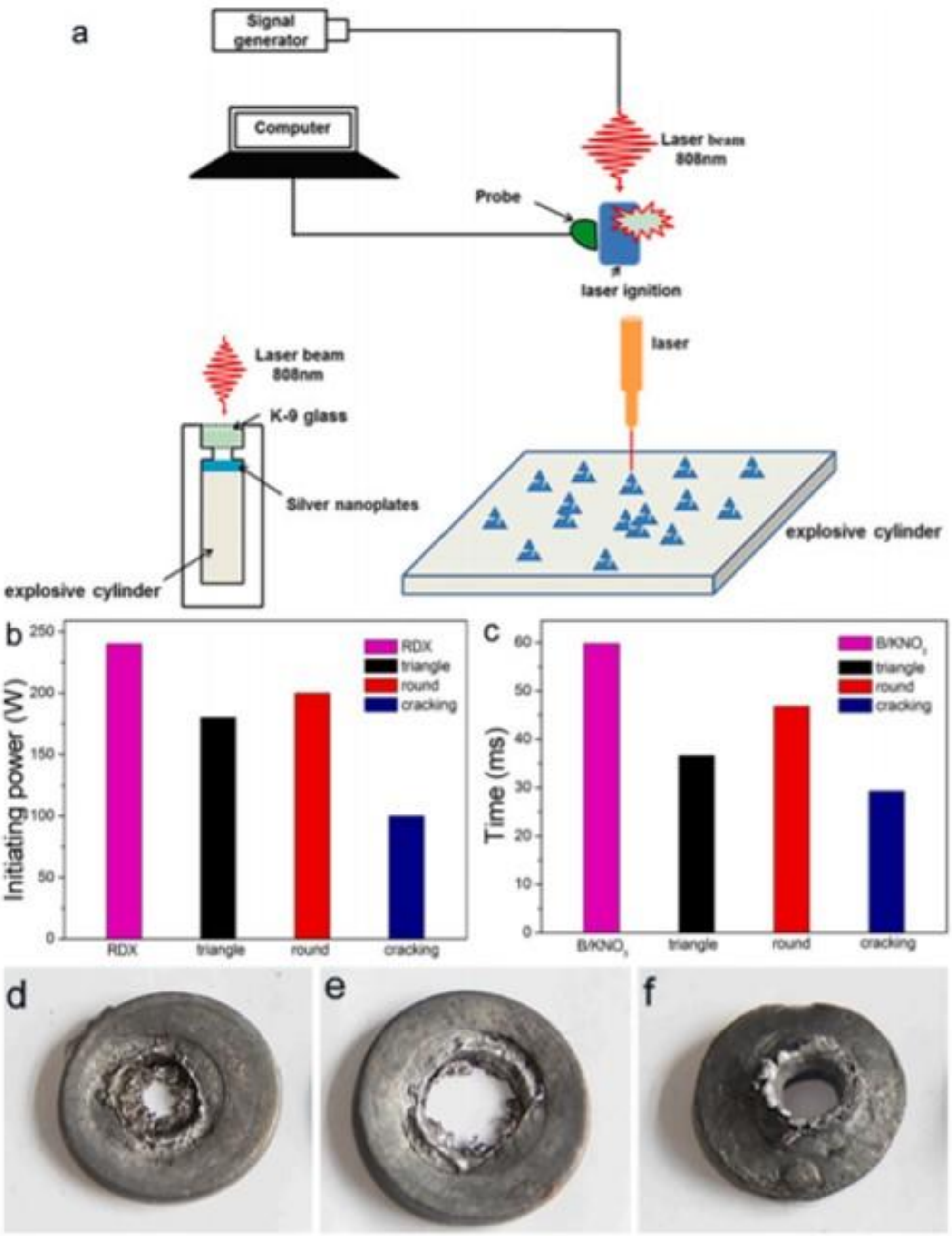

Figure 28. Thermoplasmonic detonation of insensitive high explosives [41]

5. Conclusions

The field of thermoplasmonics is a rich field of potential research and commercial relevance where metallic nanostructures can be utilized to generate confined sources of nano-heat through joule heating from optical irradiation of the metallic nanostructures, either with a laser beam, broad band flash lamps, or concentrating solar irradiation. By tuning the shape, size, and distribution of the metallic nanostructures, the absorption and scattering cross sections and resonances can be tuned to fit their applications to allow for heating with lower cost initiating sources, like laser diodes or sunlight. Heating with metallic nanostructures can be imaged utilizing a variety of different optical techniques including: scanning thermal microscopy, surface enhanced Raman spectroscopy, fluorescence polarization anisotropy spectroscopy, and quadriwave shearing interferometry which probe the temperature using microfabricated thermocouples, Raman shift, fluorescence polarization, and temperature-induced refractive index change, respectively. These metallic nanostructures have applications in industries across the board including: photothermal therapy for cancer treatments, enhanced catalysis for chemical reactions, plasmonic enhanced solar thermal membrane distillation, thermophotovoltaics, photoacoustic imaging, and optical initiation of insensitive high explosives.

6. Appendix Figures

Table 3 Summary of key SPP parameters for Au, Ag, and TiN at several frequencies in the visible and NIR.

Energy (eV)	Kx (nm)	SPP (nm)	SD M (nm)	SD D (nm)	Free Space Wavelength (nm)
Au					
3.00	275	112	29	22	413
2.50	317	92.8	6	6	496
2.01	366	1726	27	126	617
1.51	523	13889	25	282	827
Ag					
3.00	207	978	22		413
2.50	289	4631	22	95	496
2.01	383	14068	22	169	617
1.51	528	81698	22	320	827
TiN					
3.00	325	140	624	60	413
2.50	340	95	378	34	496
2.00	388	267	130	79	617
1.50	531	795	79	175	827

Table 4. Summary of absorption/scattering performances @ Resonance for Au and TiN at different particle sizes

	Max E	Absorption Cross Section (nm^2)	Scattering Cross Section (nm^2)	Free Space Wavelength (nm)
Au				
5 nm	2.38	48	0.0180	521
10 nm	2.26	393	1.9417	549
25 nm	2.01	11615	2911	617
TiN				
5 nm	2.50	20	0.0037	496
10 nm	2.50	166	0.2373	496
25 nm	2.00	4167	106.930	620

Table 5. temperature change in gold and titanium nitride nanoparticles as a function of particle radius and input power

	dT (10 mW)	dT (1 W)	dT (1kW)
Au			
5 nm	30 µK	3 mK	3 K
10 nm	122 µK	12 mK	12 K
25nm	863 µK	863 mK	86 K
TiN			
5 nm	13 µK	1.3 mK	1.3 K
10 nm	52 µK	5 mK	5 K
25 nm	218 µK	218 mK	22 K

Table 6. Transient heat diffusion times for gold, silver, and titanium nitride in air, water, and glass

	Transient Time (Air)	Transient Time (Water)	Transient Time (Glass)
Au	319 ns	138 ns	6.38 ns
Ag	316 ns	137 ns	6.33 ns
TiN	259 ns	112 ns	5.17 ns

References

[1] Yu, H.; Peng, Y.; Yang, Y.; Li, Z. Plasmon-enhanced light-matter interactions. Computational Materials (2019) 45.

[2] Peyghambarian, N.; Koch, S.; Mysyrowicz, A. *Introduction to Semiconductor Optics.* Prentice Hall 1993.

[3] Binder, R. *Solid State Optics Class Notes.* University of Arizona, 2020.

[4] Wikipedia. https://en.wikipedia.org/wiki/Surface_plasmon#/media/File:Sketch_of_surface_plasmon.png. Jun 2021.

[5] Colton, J. *Lorentz Oscillator Model.* 2020. https://physics.byu.edu/faculty/colton/docs/phy442-winter20/lecture-11-Lorentz-oscillator-model.pdf. Jun 2021

[6] Johnson, P.B.; Christy, R.W. Optical constants of the noble metals, Physical Review B, 1972, 6, 4370. https://doi.org/10.1103/PhysRevB.6.4370

[7] Pflüger, J.; Fink, J.. Determination of optical constants by high-energy, electron-energy-loss spectroscopy (EELS), In *Handbook of optical constants of solids II*, Volume II, Edward D. Palik, ed. Academic Press, 1991. pp. 293-310. https://doi.org/10.1016/B978-012544415-6.50055-8

[8] J. Pflüger, J. Fink, W. Weber, K. P. Bohnen, G. Crecelius. Dielectric properties of TiC_x, TiN_x, VC_x, and VN_x from 1.5 to 40 eV determined by electron-energy-loss spectroscopy, Physical Review B, 1984, 20, 1155. https://doi.org/10.1103/PhysRevB.30.1155

[9] Cushman, C.; Smith, N.; Kaykhaii, M.; Podraza, N.; Linford, M. An Introduction in Spectroscopy Ellipsometry, Focusing on Models for Transparent Materials: the Cauchy and Sellmeier Models. *Vacuum Technology and Coating.* July 2016.

[10] West, P.; Ishii, S.; Naik, G.; Emani, N.; Shalaev, V.; Boltasseva, A. Searching for better plasmonic materials. Laser Photonics Rev, 2010 4(6), 795-808. DOI 10.1002/lpor.200900055

[11] Wikipedia. [4] Wikipedia. https://en.wikipedia.org/wiki/Surface_plasmon#/media/File:Sketch_of_surface_plasmon.png. Jun 2021.

[12] Desai, R.; Mankad, V.; Gupta, S.; Jha, P. Size of Silver Nanoparticles: UV-Visible Spectroscopy Assessment. J. Phys. Chem. B 2006, 110, 15666-15675. 10.1021/jp0608628

[13] Baffou, G.; Quidant, R.; Girard, C. Thermoplasmonics modeling: A Green's function approach. PHYSICAL REVIEW B 82, 165424 2010. DOI: 10.1103/PhysRevB.82.165424

[14] Baffou, G.; Quidant, R. Thermo-plasmonics: using metallic nanostructures as nano-sources of heat. Laser Photonics Rev, 2013, 7(2), 171–187 DOI 10.1002/lpor.201200003

[15] Boriskina, S.; Ghasemi, H.; Chen, G. Plasmonic materials for energy: From physics to Applications. Materials Today, 2013, 16(10) https://doi.org/10.1016/j.mattod.2013.09.003

[16] Bai, W.; Qin, W.; Tang, D.; Faming, J.; Chen, H.; Yang, F.; Qiao, Z.; Duan, T.; Lin, D.; He, R.; Zhu, W.; Wang, L. Constructing interparticle hotspots through cracking silver nanoplates for laser initiation of explosives. Optics & Laser Technology, 2021, 139, 106989. 10.1016/j.optlastec.2021.106989

[17] Mantri, Y.; Jokerst, J. Engineering Plasmonic Nanoparticles for Enhanced Photoacoustic Imaging. ACS Nano 2020, 14, 9408-9422. https://doi.org/10.1021/acsnano.0c05215

[18] Guillaume Baffou, Pierre Bon, Julien Savatier, Julien Polleux, Min Zhu, et al.. Thermal Imaging of Nanostructures by Quantitative Optical Phase Analysis. ACS Nano, American Chemical Society, 2012, 6 (3), pp.2452 - 2458. ff10.1021/nn2047586ff. ffhal-00729073

[19] Mutlu, M.; Kang, J.; Raza, S.; Schoen, D.; Zheng, X.; Kik, P.; Brongersma, M. Thermoplasmonic Ignition of Metal Nanoparticles. *Nano Lett.* 2018, 18, 3, 1699–1706. https://doi.org/10.1021/acs.nanolett.7b04739

[20] Papadakis, G.; Buddhiraju, S.; Zhao, Z.; Zhao, B.; Fan, S. Broadening Near-Field Emission for Performance in Thermophotovoltaics. *Nano Lett.* 2020, 20(3), 1654–1661. https://doi.org/10.1021/acs.nanolett.9b04762

[21] Ilic, O.; Jablan, M.; Joannopoulos, J.; Celanovic, I.; Soljacic, M. Overcoming the black body limit in plasmonic and graphene near-field thermophotovoltaic systems. Optics Express 2012, 20(3), A366-A384. **https://doi.org/10.1364/OE.20.00A366**

[22] Yektaparast, B.; Shirkani, H. Controlling Optical Absorption of Graphene in Near-infrared Region by Surface Plasmons. Plasmonics, 2018 13,1623–1630 https://doi.org/10.1007/s11468-017-0671-5

[23] Guler, U.; Shalaev, V.; Boltasseva, A. Nanoparticle plasmonics: going practical with transition metal nitrides. Materials Today, 2015, 18(4). https://doi.org/10.1016/j.mattod.2014.10.039

[24] Naldoni, A.; Kudshev, Z.; Mascaretti, L.; Sarmah, S.; Rej, S.; Froning, J.; Tomanec, O.; Yoo, J.; Wang, D.; Kment, S.; Montini, T.; Fornasiero, P.; Shalaev, V.; Schumki, P.; Boltasseva, A.; Zboril, R. Solar Thermoplasmonic Nanofurnace for High-Temperature Heterogeneous Catalysis. *Nano Lett.* 2020, 20(5), 3663–3672. https://doi.org/10.1021/acs.nanolett.0c00594

[25] Mascaretti, L.; Schirato, A.; Zboril, R.; Kment, S.; Schmuki, P.; Alabastro, A.; Naldoni, A. Solar steam generation of scalable ultrathin thermolasmonic TiN nanocavity arrays. Nano Energy 83 (2021) 105828. https://doi.org/10.1016/j.nanoen.2021.105828

[26] Tumkur, T.; Sokhoyan, R.; Su, M.; Ceballos-Sanchez, A.; Shirmanesh, G.; Kim, Y.; Atwater, H.; Feigenbaum, E.; Elhadj, S. Towards high laser power beam manipulation with nanophotonic materials: evaluating thin film damage performance. Optics Express, 2021, 29, 5. 7261- 7275. **https://doi.org/10.1364/OE.413843**

[27] Gong, T.; Lyu, P.; Palm, K.; Memarzadeh, S.; Munday, J.; Leite, M. Emergent Opportunities with Metallic Alloys: From Material Design to Optical Devices. Adv. Optical Mater. 2020, 2001082. DOI: 10.1002/adom.202001082

[28] Cunha, J.; Guo, T.; Koya, A.; Toma, A.; Prato, M.; Valle, G.; Alabastri, A.; Zaccaria, R. Photoinduced Temperature Gradients in Sub-wavelength Plasmonic Structures: The Thermoplasmonics of Nanocones. Adv. Optical Mater. 2020, 8, 2000568. DOI: 10.1002/adom.202000568

[29] Park Systems. https://parksystems.com/index.php/park-spm-modes/99-thermal-properties/252-scanning-thermal-microscopy-sthm, Jun 2021.

[30] Hu, S.; Liu, B.; Feng, J.; Zong, C.; Lin, K. Wang, X.; Wu, D.; Ren, B. Quantifying Surface Temperature of Thermoplasmonic Nanostructures. J. Am. Chem. Soc. 2018, 140, 13680−13686. DOI: 10.1021/jacs.8b06083

[31] Baffou, G.; Kreuzer, M.; Kulzer, F.; Quidant, R. Temperature mapping near plasmonic nanostructures using fluorescence polarization anisotropy. Optics Express, 2009, 17 (5). **https://doi.org/10.1364/OE.17.003291**

[32] Boulais, E.; Lachaine, R.; Hatef, A.; Meunier, M. Plasmonics for pulsed-laser cell nanosurgery: Fundamentals and applications. Journal of Photochemistry and Photobiology C: Photochemistry Reviews, 2013, 17, 26– 49. http://dx.doi.org/10.1016/j.jphotochemrev.2013.06.001

[33] Chehadi, Z.; Girardon, J.; Capron, M.; Dumeignnil, F.; Jradi, S. Thermolasmonic-induced energy efficient catalytic oxidation of glycerol over gold supported catalysts using visible light at ambient temperature. Applied Catalysis A, General, 2019, 572, 9-14. https://doi.org/10.1016/j.apcata.2018.12.028

[34] Baffou, G.; Quidant, R. Nanoplasmonics for chemistry. Chem. Soc. Rev., 2014, 43, 3898. DOI: 10.1039/c3cs60364d

[35] Wang, Y.; Wang, S.; Zhang, S.; Scheman, O.; Baumberg, J.; Ding, T.; Xu, H. Plasmon-directed polymerization: Regulating polymer growth with light. Nano Research 2018, 11(12): 6384–6390 https://doi.org/10.1007/s12274-018-2163-0

[36] Yen, Y.; Chen, C.; Fang, M.; Chen, Y.; Lai, C.; Hsu, C.; Wang, Y.; Lin, H.; Shen, C.; Shieh, J.; Ho, J.; Chueh, Y. Thermoplasmonics-assisted nanoheterostructured Au-decorated $CuInS_2$ nanoparticles: Matching solar spectrum absorption and its application on selective distillation of non-polar solvent systems by thermal solar energy. Nano Energy, 2015, 15, 470-478. https://doi.org/10.1016/j.nanoen.2015.04.031

[37] Politano, A.; Profio, G.; Fontananova, E.; Sanna, V. Cupolilo, A. Curcio, E. Overcoming temperature polarization in membrance distillation by thermoplasmonic effects activated by Ag nanofillers in polymeric membranes. Desalination, 2019, 451 192-199. https://doi.org/10.1016/j.desal.2018.03.006

[38] Politano, A.; Argurio, P.; Profio, G.; Sanna, V.; Cupolillo, A.; Chakraborty, S.; Arafat, H.; Curcio, E. Photothermal Membrane Distillation for Seawater Desalination. Adv. Mater. 2017, 29, 1603504. **https://doi.org/10.1002/adma.201603504**

[39] Churchyard, S.; Fang, X.; Vrcelj, R. Laser ignitibility of energetic crystals doped with gold nanoparticles. Optics and Laser Technology, 2019, 113 281-288. https://doi.org/10.1016/j.optlastec.2018.12.021

[40] Fang, X.; Sharma, M.; Stennet, C.; Gill, P. Optical sensitization of energetic crystals with gold nanoparticles for laser ignition. Combustion and Flame, 2017, 183 15-21. DOI:10.1016/J.COMBUSTFLAME.2017.05.002